

5-1-2023

Differential regulation of cardiac sodium channels by intracellular fibroblast growth factors

Paweorn Angsutrarux
Washington University in St. Louis

Amal K Dutta
Washington University School of Medicine in St. Louis

Martina Marras
Washington University in St. Louis

Carlota Abella
Washington University in St. Louis

Rebecca L Mellor
Washington University School of Medicine in St. Louis

See next page for additional authors

Follow this and additional works at: https://digitalcommons.wustl.edu/oa_4



Part of the [Medicine and Health Sciences Commons](#)

Please let us know how this document benefits you.

Recommended Citation

Angsutrarux, Paweorn; Dutta, Amal K; Marras, Martina; Abella, Carlota; Mellor, Rebecca L; Shi, Jingyi; Nerbonne, Jeanne M; and Silva, Jonathan R, "Differential regulation of cardiac sodium channels by intracellular fibroblast growth factors." *Journal of general physiology*. 155, 5. e202213300 (2023).
https://digitalcommons.wustl.edu/oa_4/1532



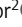
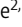

This Open Access Publication is brought to you for free and open access by the Open Access Publications at Digital Commons@Becker. It has been accepted for inclusion in 2020-Current year OA Pubs by an authorized administrator of Digital Commons@Becker. For more information, please contact vanam@wustl.edu.

Authors

Paweorn Angsutararux, Amal K Dutta, Martina Marras, Carlota Abella, Rebecca L Mellor, Jingyi Shi, Jeanne M Nerbonne, and Jonathan R Silva

ARTICLE

Differential regulation of cardiac sodium channels by intracellular fibroblast growth factors

Paweorn Angsutararux¹, Amal K. Dutta², Martina Marras¹, Carlota Abella¹, Rebecca L. Mellor², Jingyi Shi¹, Jeanne M. Nerbonne^{2,3}, and Jonathan R. Silva¹

Voltage-gated sodium (Na_v) channels are responsible for the initiation and propagation of action potentials. In the heart, the predominant Na_v1.5 α subunit is composed of four homologous repeats (I–IV) and forms a macromolecular complex with multiple accessory proteins, including intracellular fibroblast growth factors (iFGF). In spite of high homology, each of the iFGFs, iFGF11–iFGF14, as well as the individual iFGF splice variants, differentially regulates Na_v channel gating, and the mechanisms underlying these differential effects remain elusive. Much of the work exploring iFGF regulation of Na_v1.5 has been performed in mouse and rat ventricular myocytes in which iFGF13VY is the predominant iFGF expressed, whereas investigation into Na_v1.5 regulation by the human heart-dominant iFGF12B is lacking. In this study, we used a mouse model with cardiac-specific *Fgf13* deletion to study the consequences of iFGF13VY and iFGF12B expression. We observed distinct effects on the voltage-dependences of activation and inactivation of the sodium currents (I_{Na}), as well as on the kinetics of peak I_{Na} decay. Results in native myocytes were recapitulated with human Na_v1.5 heterologously expressed in *Xenopus* oocytes, and additional experiments using voltage-clamp fluorometry (VCF) revealed iFGF-specific effects on the activation of the Na_v1.5 voltage sensor domain in repeat IV (VSD-IV). iFGF chimeras further unveiled roles for all three iFGF domains (i.e., the N-terminus, core, and C-terminus) on the regulation of VSD-IV, and a slower time domain of inactivation. We present here a novel mechanism of iFGF regulation that is specific to individual iFGF isoforms and that leads to distinct functional effects on Na_v channel/current kinetics.

Introduction

In the heart, voltage-gated sodium (Na_v) channels are responsible for the rapid upstroke of action potentials (APs) in atrial and ventricular myocytes, and in Purkinje fibers (Nerbonne and Kass, 2005). The predominant Na_v channel pore-forming (α) subunit responsible for generating these channels in the mammalian myocardium is Na_v1.5 (Abriel and Kass, 2005). Precise regulation of Na_v1.5 gating is essential for the proper electro-mechanical functioning of the heart and the disruption of gating in acquired and inherited cardiac diseases predisposes individuals to potentially life-threatening arrhythmias (Noble and Noble, 2006; Mangold et al, 2017; Ton et al, 2021). Mutations in *SCN5A*, the gene which encodes Na_v1.5, for example, are linked to congenital cardiac arrhythmia syndromes, including the long QT type 3 (LQT3) and Brugada syndromes (Ruan et al., 2009). Similar to other Na_v α-subunits, Na_v1.5 has four homologous repeats (I–IV), each of which contains six α-helical

transmembrane segments (S1–S6; Yu and Catterall, 2003). The S1–S4 segments in each repeat form the voltage sensor domains VSD-I through VSD-IV, and the S5–S6 segments in the four repeats combine to constitute the Na⁺-selective pore. The activation of each VSD on membrane depolarization is coupled to conformational changes in the channel, leading to a rapid opening of the activation gate, followed closely by channel inactivation (Varga et al., 2015).

Native myocardial Na_v channels function in macromolecular complexes, comprising the Na_v1.5 α-subunit and various auxiliary subunits, including Na_v β-subunits (Calhoun and Isom, 2014), calmodulin (CaM; Gardill et al, 2019), and intracellular fibroblast growth factors (iFGFs; Yang et al., 2016; Pitt and Lee, 2016) that influence channel stability, trafficking, and biophysical properties (Abriel and Kass, 2005; Meadows and Isom, 2005; Abriel, 2010). It has been previously demonstrated that

¹Department of Biomedical Engineering, McKelvey School of Engineering, Washington University in St. Louis, St. Louis, MO, USA; ²Department of Medicine, Cardiovascular Division, Washington University School of Medicine, St. Louis, MO, USA; ³Department of Developmental Biology, Washington University School of Medicine, St. Louis, MO, USA.

Correspondence to Jonathan R. Silva: jonsilva@wustl.edu; Jeanne M. Nerbonne: jnerbonne@wustl.edu

This work is part of a special issue on Structure and Function of Ion Channels in Native Cells and Macromolecular Complexes.

© 2023 Angsutararux et al. This article is distributed under the terms of an Attribution–Noncommercial–Share Alike–No Mirror Sites license for the first six months after the publication date (see <http://www.rupress.org/terms/>). After six months it is available under a Creative Commons License (Attribution–Noncommercial–Share Alike 4.0 International license, as described at <https://creativecommons.org/licenses/by-nc-sa/4.0/>).

the auxiliary β -subunits differentially regulate the expression, gating, and pharmacological sensitivity of Na_v channels (Dhar Malhotra et al., 2001; Zhu et al., 2017; Angsutararux et al., 2021b). Although less well-studied, iFGFs have been shown to bind to the C-terminal domain of Na_v α -subunits, including $\text{Na}_v1.5$, and to modulate the time- and voltage-dependent properties of heterologously expressed (Liu et al., 2001; Liu et al., 2003) and native (Pablo and Pitt, 2017; Goldfarb et al., 2007) $\text{Na}_v1.5$ -encoded currents.

The iFGFs, also known as fibroblast growth factor homologous factors (FHF), are a subfamily of FGFs, consisting of iFGF11–iFGF14 that have similar “core” sequences and distinct N-termini (Olsen et al., 2003; Goldfarb, 2005). Alternative exon usage and differential N-terminal splicing generate further iFGF protein diversity (Munoz-Sanjuan et al., 2000; Pablo and Pitt, 2017). The crystal structure of the $\text{Na}_v1.5$ C-terminus in complex with iFGF13 and CaM revealed that the binding of iFGF13 is mediated by amino acids in the core domain (Wang et al., 2012; Musa et al., 2015; Hennessey et al., 2013). The earlier structure of iFGF12 alone (Goetz et al., 2009) and the later structure of iFGF12B in complex with $\text{Na}_v1.5$ C-terminus and CaM (Wang et al., 2014) reveal iFGF12 structures nearly identical to iFGF13, especially in the core region. Although these findings suggest that all iFGFs might modulate the properties of Na_v channels encoded by a given Na_v α -subunit (such as $\text{Na}_v1.5$) similarly, this is not the case. Indeed, various iFGF proteins have been shown to exert dramatically different effects on the gating of Na_v channels that depend on both the subtype of Na_v α -subunit and the specific isoform of iFGF (Munoz-Sanjuan et al., 2000; Liu et al., 2003; Goetz et al., 2009; Wang et al., 2011b; Chakouri et al., 2022). For example, three iFGF13 splice variants, iFGF13S (iFGF13A), iFGF13U (iFGF13B), and iFGF13VY, were shown to produce distinct effects on the gating of $\text{Na}_v1.5$ channels (Yang et al., 2016). Two iFGF14 isoforms, iFGF14A and iFGF14B, have also been shown to differentially modulate $\text{Na}_v1.5$ -encoded currents and to produce functional effects markedly different from iFGF13-mediated effects (Lou et al., 2005).

The most prominent iFGF expressed in the human heart, iFGF12B, has been linked to inherited cardiac arrhythmias (Hennessey et al., 2013; Li et al., 2017). In addition, LQT3 and Brugada syndrome-linked mutations in $\text{Na}_v1.5$ have been shown to disrupt iFGF binding and/or to modify iFGF-mediated effects on the properties of $\text{Na}_v1.5$ -encoded currents (Musa et al., 2015; Liu et al., 2003). The mechanisms underlying iFGF12B-mediated regulation of cardiac $\text{Na}_v1.5$ channels, however, have not been defined. The experiments here were designed to address this knowledge gap and, in addition, to directly compare the effects of iFGF12B on cardiac $\text{Na}_v1.5$ channels with those of the extensively studied iFGF13VY, the predominant iFGF expressed in rodent ventricles (Wang et al., 2011a; Park et al., 2016).

Materials and Methods

Experimental animals

Adult (8–20-wk-old) male and female wild-type (WT), *Fgf12KO*, *Fgf13 floxed*, and *cFgf13KO* C57BL/6J mice were used in the experiments here. The *Fgf12KO* line (Goldfarb et al., 2007) was

obtained from Drs. Mitchell Goldfarb (City University of New York, New York, NY) and David Ornitz (Washington University School of Medicine, St. Louis, MO). The *Fgf13 floxed* and *cFgf13KO* lines were generated as described below. The transgenic C57BL/6J mouse line (Tg(Myh6-cre)2182Mds), expressing Cre-recombinase driven by the cardiac-specific α -myosin heavy chain (α -MHC) promoter, was purchased from The Jackson Laboratory. Adult female *Xenopus laevis* of sizes >9 cm were obtained from Xenopus 1 Corp, and oocytes were harvested using previously described methods (Varga et al., 2015). All animals were handled in accordance with the National Institutes of Health (NIH) Guide for the Care and Use of Laboratory Animals, and all experimental protocols were approved by the Washington University Institutional Animal Care and Use Committee (IACUC).

Generation and validation of mice with cardiac specific deletion of *Fgf13* (*cFgf13KO*)

To enable conditional deletion of *Fgf13*, mice in which the *Fgf13* locus (on the X chromosome) was floxed were generated by the Genome Editing and Stem Cell (GESC) Center in the McDonnell Genome Institute and the Mouse Genetics Core at Washington University using CRISPR-Cas9 gene editing technology (Doudna and Charpentier, 2014), modified to provide robust and reliable generation of floxed alleles (Sentmanat et al., 2022). Briefly, guide RNAs (gRNAs) and single-stranded oligodeoxynucleotides (ssODNs) were designed to introduce a 5'-side LoxP (5' LoxP) site into the intron upstream of exon 2 and a 3'-side LoxP (3' LoxP) site into the intron downstream of exon three of the *Fgf13* gene (Fig. S1 A). These gRNAs and ssODNs, together with Cas9, were electroporated into single-cell C57BL/6J embryos, and these embryos were transferred into the oviducts of pseudo-pregnant females, ~20 embryos per recipient.

Following preliminary screening of the founder (F0 generation) pups, proper insertion and localization of the loxP sites were confirmed by sequencing. To ensure germline transmission and that both loxP sites were on the same allele, F0 animals positive for both loxP sites were crossed to WT C57BL/6J animals and the resulting (F1 generation) offspring were also screened by sequencing. Heterozygous *Fgf13* floxed (*Fgf13^{fl/+}*) female and hemizygous *Fgf13* floxed (*Fgf13^{fl/y}*) male (F1) offspring were mated to produce (F2) females homozygous for the floxed *Fgf13* locus, *Fgf13^{fl/fl}* (Fig. S1 A). The *Fgf13^{fl/fl}* and *Fgf13^{fl/y}* animals were then crossed with transgenic animals (Tg(Myh6-cre)2182Mds) expressing Cre-recombinase driven by the (cardiac specific) α -MHC promoter (Fig. S1 A). Crossing Cre-recombinase-expressing hemizygous male (*Fgf13^{fl/y}*) offspring with *Fgf13^{fl/fl}* females (or Cre-recombinase-expressing heterozygous *Fgf13^{fl/+}* females with *Fgf13^{fl/y}* males) provided cardiac-specific *Fgf13* targeted deletion hemizygous male (*cFgf13^{-/y}*) and homozygous female (*cFgf13^{-/-}*) animals, referred to here collectively as cardiac-specific *Fgf13* knockouts, *cFgf13KO*. Offspring (from this and subsequent crosses) were screened by PCR using the primers given in Table S1 A, and representative results are illustrated in Fig. S1 B.

To confirm the elimination of the iFGF13 protein in the myocardium of *cFgf13KO* animals, protein lysates were prepared

from WT and *cFgf13KO* left ventricles (LVs). Following protein fractionation and transfer, membranes were probed with a polyclonal anti-FGF13 antibody (generously provided by Dr. Geoffrey Pitt, Weill Cornell Medical School, New York, NY). As illustrated in Fig. S1 C (left panel), two bands, at ~32 and ~24 kD, were detected with the anti-iFGF13 antibody in the WT LV samples, whereas these bands were not detected in the *cFgf13KO* LV samples, consistent with the elimination of the iFGF13 protein. Similar analyses, conducted on LV protein lysates prepared from *Fgf12KO* animals, revealed iFGF13 protein expression indistinguishable from that observed in WT LV (Fig. S1 C, right panel).

AAV vector production

AAV9 vectors were prepared by the Hope Center Viral Vectors Core at Washington University, as described previously (Zolotukhin et al, 2002). Briefly, HEK-293 cells, maintained in Dulbecco's modified Eagle's medium (DMEM), supplemented with 5% fetal bovine serum (FBS), 100 U/ml penicillin, and 100 µg/ml streptomycin at 37°C in a 95% air/5% CO₂ incubator, were plated at 30–40% confluence in CellSTACS (Corning). Approximately 24 h later, cells were cotransfected with 0.6 mg of the AAV transfer plasmid containing the construct of interest (e.g., human iFGF12B, hFGF12B) and 1.8 mg of a helper plasmid (pXYZ1) using the calcium phosphate precipitation method (Zolotukhin et al, 2002). The transfection medium was removed after 6 h, and the cells were incubated at 37°C for 3 d. For harvesting, cells were lysed by three freeze/thaw cycles and the cell lysates were collected and treated with 50 U/ml of Benzonase, followed by iodixanol gradient centrifugation. The iodixanol gradient fraction was further purified on a HiTrap Q column and concentrated (Zolotukhin et al, 2002). The vector titer of hFGF12B, determined by Dot blot assay, was 3.8×10^{13} vg/ml (viral genomes/ml).

Virus injections

Adult (8–12 wk) male and female WT and *cFgf13KO* C57BL/6J mice were anesthetized by intraperitoneal (ip) injection of 1 ml/kg of a ketamine/xylene (30 mg/ml/4 mg/ml) cocktail; the body temperature was maintained at 37°C with a feedback-controlled heating pad. Each animal was placed on its left side with the head facing to the right, and virus injections were made into the right retro-orbital sinus. Gentle downward pressure was applied to the skin dorsal and ventral to the eye, making the eye protrude slightly. Retro-orbital injection of a 1:1 mixture of the hFGF12B-expressing (20 µl) and the eGFP-expressing AAV9 (20 µl) viruses was then made. For injections, the virus solution (20–40 µl) was drawn up into an (0.5 ml) insulin syringe and the (12.7 mm) syringe needle was then placed at the medial canthus of the eye at an angle of ~30° and with the bevel facing down. After inserting the needle until it reached the back of the orbit, the virus solution was injected (10 µl/min) slowly. The needle was then gently and slowly removed to prevent damage to the eye. The grips around the eye were then released, the eyelid was closed, and mild pressure was applied to the injection site for a few seconds. Animals were monitored for ~2 h to ensure that there were no unexpected deleterious effects of the anesthesia or the injections and were then returned to their home cages.

To confirm the expression of iFGF12 and determine the time course of eGFP/iFGF12 expression in the ventricles of virus-injected animals, protein lysates were prepared from *cFgf13KO* LV at 2, 3, and 4 wk following the injections of the hFGF12B-expressing and eGFP-expressing AAV9 viruses. Following protein fractionation and transfer, membranes were probed with a polyclonal anti-eGFP antibody (Fig. S4 A) or with a polyclonal anti-iFGF12 antibody (Fig. S4 B). The anti-iFGF12 antibody was validated using protein lysates prepared from WT and *Fgf12KO* adult mouse left and right atria. A prominent band at ~20 kD was detected with the anti-iFGF12 antibody in the WT, but not in the *Fgf12KO*, atrial protein samples (Fig. S4 C), consistent with the elimination of iFGF12 proteins and validating the anti-FGF12 antibody for Western blot analyses of iFGF12 protein expression.

Xenopus oocyte expression constructs

cDNAs encoding human *SCN5A*, *Fgf12B*, and *Fgf13VY* were produced from pMAX and pBSTA vectors accordingly. Point mutations were made in the *SCN5A* gene using the QuikChange II site-directed mutagenesis kit (Agilent) with primers from Sigma-Aldrich containing the mutation. The DNA constructs of the iFGF chimeras were synthesized by GeneArt Gene Synthesis (Thermo Fisher Scientific). All mutations and chimeras were confirmed by sequencing. Complementary RNAs (cRNAs) were synthesized with the mMessage mMACHINE T7 Transcription kit (Life Technologies) after linearizing the corresponding cDNAs with the appropriate restriction enzyme and purifying with the NucleoSpin Gel and PCR Clean-up kit (Macherey-Nagel). Each cRNA was reconstituted with double-distilled H₂O at a concentration of ~1 µg/µl.

Myocyte isolation

Myocytes were isolated from the LV of adult (10–20-wk-old) male and female WT, *Fgf13* floxed (female *Fgf13^{fl/fl}* and male *Fgf13^{fl/y}*), *cFgf13KO* (female *cFgf13^{-/-}* and male *cFgf13^{-/y}*), and *Fgf12KO* mice by enzymatic and mechanical dissociation using previously described methods (Xu et al. 1999; Brunet et al., 2004). In addition, LV myocytes were isolated from *cFgf13KO* mice (4–6 wk) after retro-orbital (eGFP- + FGF12B-expressing) AAV9 injections. Briefly, hearts were quickly removed from avertin-anesthetized mice and perfused retrogradely through the aorta with collagenase-containing solution (Type II, Worthington) at 37°C. After 15–20 min perfusion, the LV was separated, minced, and dispersed by gentle trituration. The resulting cell suspension was filtered and resuspended in serum-free medium-199 (M-199; Sigma-Aldrich). Isolated myocytes were plated on laminin-coated coverslips and maintained in a 95% air-5% CO₂ incubator at 37°C until used (within 24–48 h) in electrophysiological experiments.

Na_v current (I_{Na}) recordings from adult mouse LV myocytes

Whole-cell voltage-clamp recordings were obtained from adult mouse LV myocytes within 24–36 h of isolation at room temperature (22–24°C) using an Axopatch 1D (Axon Instruments) amplifier interfaced with a Digidata 1332 data acquisition system (Axon Instruments) and the pClamp 10 (Axon Instruments) software to a Dell computer. Recording pipettes contained

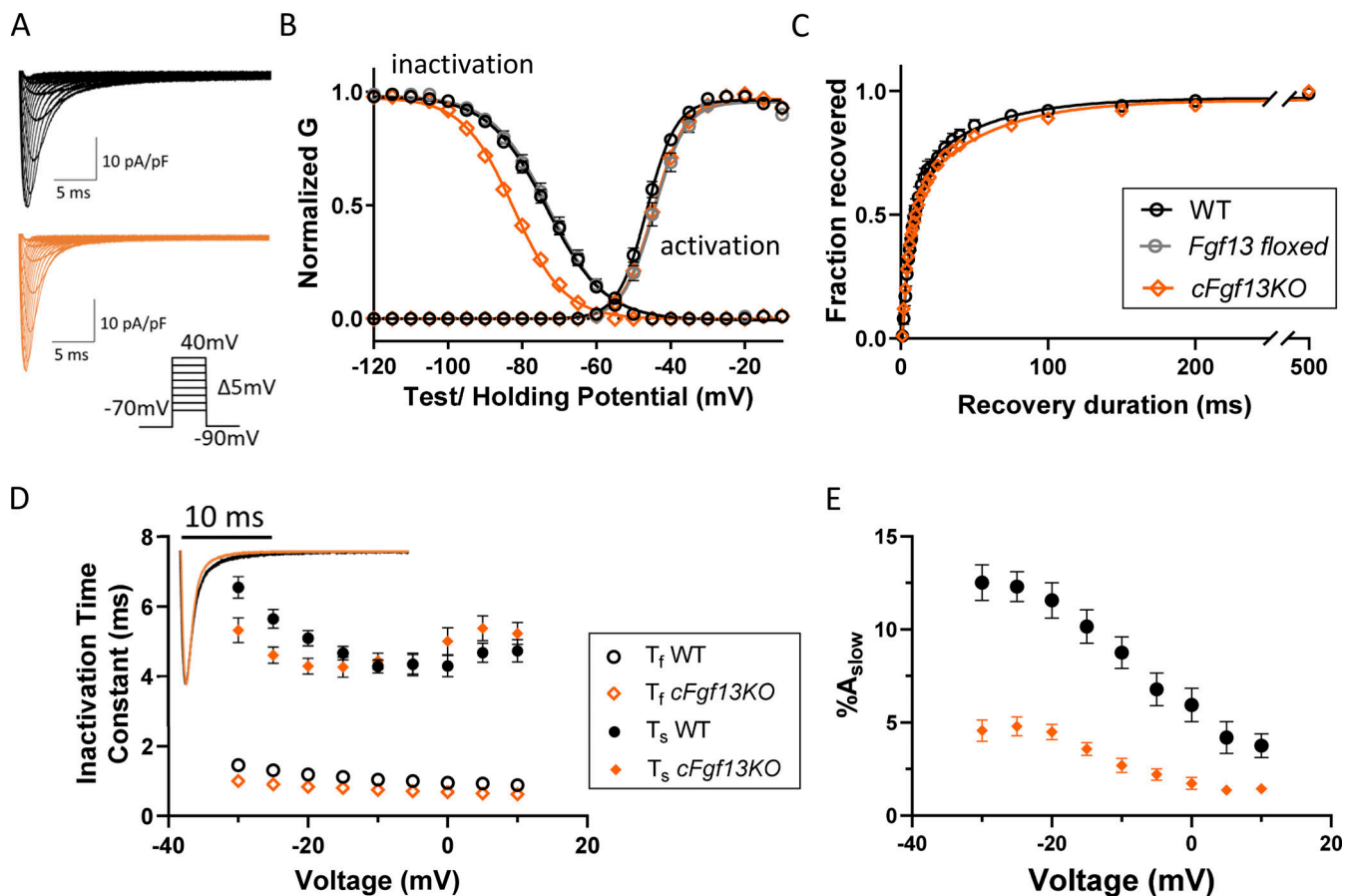


Figure 1. Cardiac-specific deletion of *Fgf13* (*cFgf13KO*) alters inactivation, but not activation, of I_{Na} in LV myocytes. (A) Representative I_{Na} waveforms recorded from LV myocytes isolated from WT (black) and cardiac-specific *Fgf13* deletion (*cFgf13KO*; orange) mice; the voltage-clamp protocol is illustrated below the current records. (B) Mean \pm SEM normalized conductances (G) of I_{Na} activation and inactivation were plotted as a function of voltage and fitted to single Boltzmann functions (solid lines). There is a marked hyperpolarizing shift in the voltage-dependence of I_{Na} inactivation in *cFgf13KO* (orange) compared with WT (black) LV myocytes (P value < 0.001 ; Table 1), whereas the voltage-dependences of I_{Na} activation are indistinguishable in *cFgf13KO* and WT LV myocytes (P value = 0.12; Table 1). Control experiments revealed that the voltage-dependences of I_{Na} activation and inactivation in *Fgf13 floxed* (grey) LV myocytes are indistinguishable from WT LV myocytes (P values are 0.11 and 0.97, respectively; Table 1). It was not possible, however, to conduct additional control experiments to independently determine if there are any of the previously reported cardiotoxic effects (Pugach et al., 2015) of the prolonged expression of Cre-recombinase in our *cFgf13KO* mice. (C) Analysis of I_{Na} recovery from inactivation, examined using a three-step protocol as described in Materials and methods, reveals that recovery follows a biexponential time course (see Table 1). The decay phases of I_{Na} in all WT adult mouse LV myocytes were best fitted with the sum of two exponentials as described in Materials and methods. (D) The mean \pm SEM ($n = 19$) fast (T_f) and slow (T_s) time constants of I_{Na} decay determined in WT cells are plotted as a function of the test potentials in D. As is evident, neither time constant displays any appreciable voltage dependence (P value = 0.26; Table 1). Inset: Overlaying representative I_{Na} waveforms recorded from *cFgf13KO* and WT LV myocytes reveal that current decay is accelerated in *cFgf13KO* compared with WT cells. Indeed, in 13 (of 26) *cFgf13KO* LV myocytes, the decay phases of I_{Na} were best described by single exponentials characterized by T values indistinguishable from T_f determined in WT cells, i.e., the slow component of I_{Na} decay was undetectable in these 13 cells. For the remaining 13 (of 26) *cFgf13KO* LV myocytes, I_{Na} decay was well described by two exponentials, with T_f and T_s values similar to those determined in WT cells at all test potentials (see values in Table S2). (E) The mean \pm SEM fractional amplitudes of the slow component of I_{Na} decay ($\%A_{slow}$) in these (13 of 26) *cFgf13KO* LV myocytes, however, were significantly lower than those determined in WT cells at all test potentials (see values in Table S2).

(in mM) 90 CsCH₃O₃S, 20 CsCl, 5 NaCl, 5 MgATP, 0.4 TrisGTP, 10 EGTA, and 10 HEPES (pH 7.3; 300 mOsm). Pipette resistances were routinely 1.5–3.0 M Ω when filled with the recording solution. The bath solution contained (in mM) 20 NaCl, 65 CsCl, 50 TEACl; 2 MgCl₂, 1 CaCl₂, 0.5 CdCl₂, 10 HEPES, and 10 glucose (pH 7.3; 310 mOsm).

Electrophysiological data were acquired at 100 KHz and signals were low-pass filtered at 5 kHz prior to digitization and storage. After the formation of a gigaohm-seal (> 1 G Ω) and establishment of the whole-cell configuration, brief (10 ms) \pm 10 mV voltage steps from the holding potential (HP) of -90 mV

were presented to allow measurements of whole-cell membrane capacitances (C_m), input resistances (R_{in}), and series resistances (R_s). In each cell, C_m and R_s were compensated electronically by $\sim 85\%$; voltage errors resulting from uncompensated series resistances were always < 2 mV and were not corrected. Leak currents were always < 50 pA and were not corrected.

To determine the voltage-dependences of activation of I_{Na} in isolated adult WT, *Fgf13 floxed*, *cFgf13KO*, *Fgf12KO*, and eGFP- + hFGF12B-expressing *cFgf13KO* LV myocytes, whole-cell I_{Na} , evoked in response to voltage steps to various test potentials (ranging from -70 mV to $+40$ mV in 5 mV increments) from a

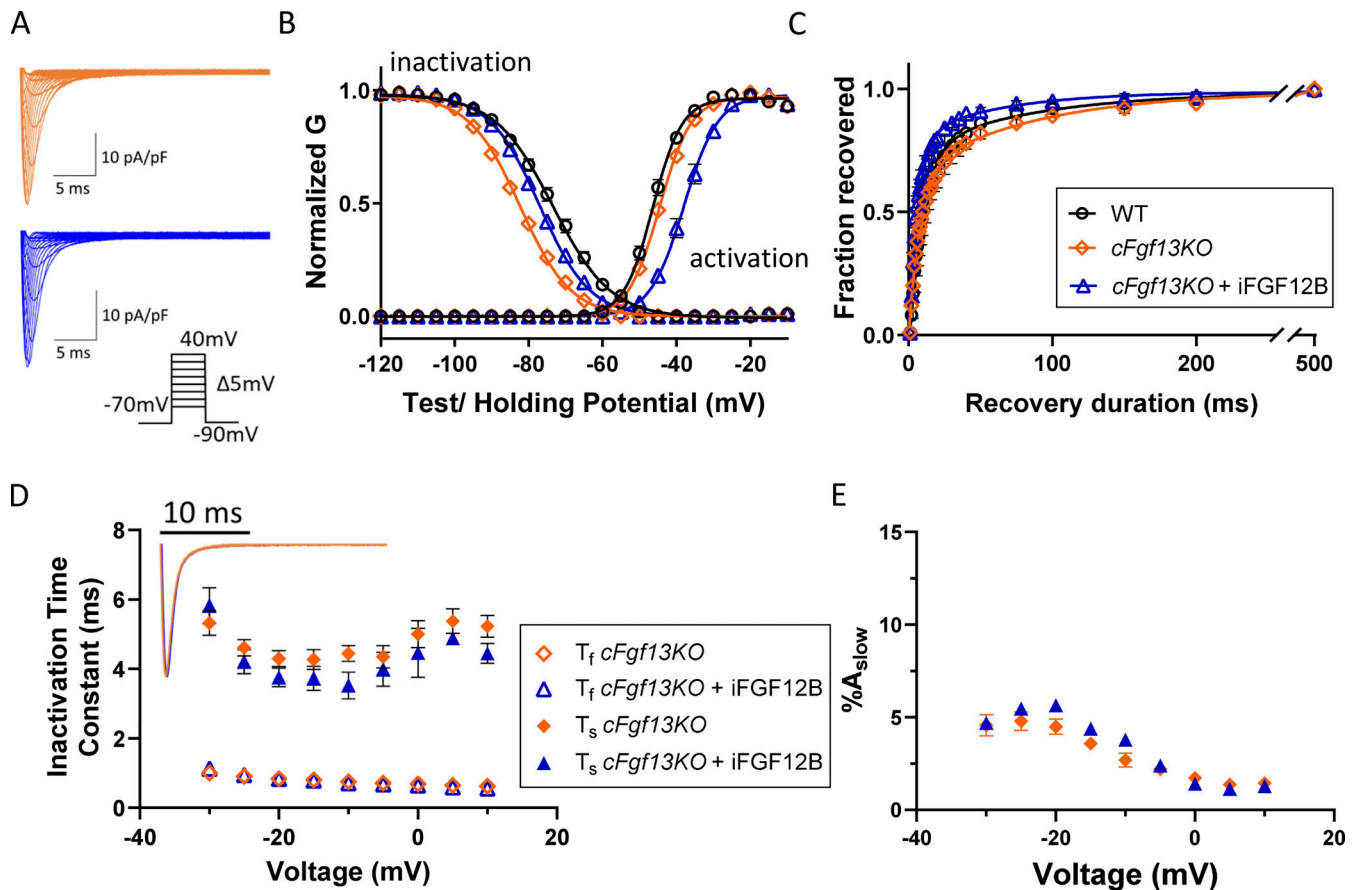


Figure 2. Expression of iFGF12B in *cFgf13KO* LV myocytes alters the voltage-dependence of I_{Na} activation and inactivation. (A) Representative I_{Na} waveforms recorded from *cFgf13KO* LV myocytes without (orange) and with (blue) iFGF12B expression; the voltage-clamp protocol is illustrated below the current records. (B) The expression of iFGF12B in *cFgf13KO* LV myocytes resulted in depolarizing shifts in I_{Na} activation and inactivation (blue) compared with *cFgf13KO* LV myocytes (orange; P values are <0.001 for both G-V activation and inactivation; Table 1). (C) Expression of iFGF12B in *cFgf13KO* LV myocytes also accelerated I_{Na} recovery from inactivation compared with the currents in both WT and *cFgf13KO* LV myocytes (P value = 0.04; Table 1). (D) The decay phases of the currents in *cFgf13KO* cells expressing iFGF12B (blue), however, are indistinguishable from *cFgf13KO* (orange) LV myocytes (inset). In addition, in 13 (of 19) *cFgf13KO* + iFGF12B-expressing LV myocytes, the decay phases of I_{Na} were best described by single exponentials with τ values indistinguishable from τ_f determined in WT cells, i.e., the slow component of I_{Na} decay was undetectable in these 13 cells. In the remaining (6 of 19) *cFgf13KO* + iFGF12B-expressing LV myocytes, I_{Na} decay was well described by the sum of two exponentials (D) with τ_f and τ_s values similar to those in *cFgf13KO* and WT (Fig. 1 D) cells (see values in Table S2). (E) In addition, the fractional amplitudes of the slow component of I_{Na} decay ($\%A_{slow}$) in *cFgf13KO* + iFGF12B-expressing LV myocytes are indistinguishable at all test potentials from those determined in *cFgf13KO* cells (see values in Table S2).

HP of -90 mV, were recorded. Representative records are shown in Figs. 1 and 2. C_m values were determined by integration of the capacitive transients recorded during ± 10 mV voltage steps from -90 mV. Peak I_{Na} was defined as the maximal amplitudes of the currents recorded during each voltage step. Current amplitudes in each cell were normalized to the cell capacitance and current densities are reported (pA/pF). Transient Na_v conductances (G_{Na}) in each cell at each test potential were calculated and normalized to the maximal peak Na_v conductance ($G_{Na,max}$) measured in the same cell. Mean \pm SEM normalized peak Na_v conductances ($G_{Na}/G_{Na,max}$), determined in WT, *Fgf13 floxed*, *cFgf13KO*, *Fgf12KO*, and hFGF12B- + eGFP-expressing *cFgf13KO* LV myocytes were plotted as a function of the test potential (V_m) and fitted using the Boltzmann equation (Eq. 1):

$$G(V) = 1 / \{1 + \exp[-(V - V_{1/2})/k]\}, \quad (1)$$

where $V_{1/2}$ is the half-activation voltage and k is the slope factor.

The decay phases of I_{Na} evoked at each test potential in all WT LV myocytes were well-fitted by the sum of two exponentials (Eq. 2):

$$I(t) = \text{constant} - a_f \exp(t/\tau_f) - a_s \exp(t/\tau_s), \quad (2)$$

where a_f and a_s are the amplitudes of the fast and slow components of inactivation, and τ_f and τ_s are time constants of inactivation. Similar analyses of the decay phases of the currents in *cFgf13KO* and iFGF12B + eGFP-expressing *cFgf13KO* LV myocytes revealed that the decay phases of the currents in many of the cells (see Results) were not well-fitted by the sum of two exponentials. Rather, the decay phases of I_{Na} in these cells were well-described by single exponentials with τ values similar to the fast component (τ_f) determined in WT cells. For all cells in which two exponentials were required, the fractional amplitude of the slow component ($\%A_{slow}$) at each test potential was calculated as $a_s / (a_f + a_s)$. The mean \pm SEM τ_f and τ_s values and the

mean \pm SEM fractional amplitudes of the slow component of I_{NaV} current decay in all WT cells and in the *cFgf13KO* and *hFGF12B*- + eGFP-expressing *cFgf13KO* LV myocytes well described by two exponentials are presented (see Results).

To determine the voltage-dependences of steady-state inactivation of I_{Na} in WT, *Fgf13* floxed, *cFgf13KO*, *Fgf12KO*, and eGFP- + *hFGF12B*-expressing *cFgf13KO* LV myocytes, whole-cell I_{NaV} currents, evoked at -30 mV following brief (25 ms) conditioning voltage steps (ranging from -130 to -15 mV in 5 mV increments), presented from a HP of -90 mV, were recorded. Peak I_{Na} , evoked at -30 mV from each conditioning potential in each cell, was measured and normalized to the maximal peak current ($I_{Na,max}$) evoked (in the same cell) from the most hyperpolarized conditioning potential (of -130 mV). Mean \pm SEM normalized current amplitudes ($I_{Na}/I_{Na,max}$), determined in WT, *Fgf13* floxed, *cFgf13KO*, *Fgf12KO*, and *hFGF12B*- + eGFP-expressing *cFgf13KO* LV myocytes, were then plotted as a function of the conditioning membrane potential (V_m) and fitted using the Boltzmann equation (Eq. 1).

To examine the kinetics of I_{Na} recovery from inactivation, a three-pulse voltage-clamp protocol was used. LV myocytes were first depolarized to -30 mV from a HP of -90 mV to evoke inward currents and subsequently hyperpolarized to -90 mV for various times, ranging from 1 ms to 3 s, followed by a second depolarizing step to -30 mV to again evoke inward currents and assess the extent of recovery. Peak I_{Na} amplitudes evoked following each test interval were measured and normalized to the amplitude of the peak I_{Na} recorded (in the same cell) during the initial depolarizing voltage step. Mean \pm SEM normalized peak I_{Na} amplitudes in WT, *cFgf13KO*, and *hFGF12B*- + eGFP-expressing *cFgf13KO* LV myocytes were then determined and plotted as a function of the recovery interval. The normalized recovery data were fitted with double exponentials (Eq. 3):

$$I(t) = \text{constant} - a_1 \exp(t/\tau_{R,1}) - a_2 \exp(t/\tau_{R,2}), \quad (3)$$

where a_1 and a_2 are the current amplitudes at non-zero recovery, and $\tau_{R,1}$ and $\tau_{R,2}$ are the recovery time constants. Whole-cell voltage-clamp data were compiled and analyzed using Clampfit (Molecular Devices), Microsoft Excel, and Prism (GraphPad).

Cut-open oocyte voltage-clamp and voltage-clamp fluorometry (VCF)

Harvested oocytes were then digested into single cells with collagenase (Sigma-Aldrich). Oocytes were injected with cRNAs and incubated in ND93 solution (93 mM NaCl, 5 mM KCl, 1.8 mM $CaCl_2$, 1 mM $MgCl_2$, 5 mM HEPES, 2.5 mM Na pyruvate, and 1% penicillin/streptomycin, pH 7.4) at $18^\circ C$ for 3–6 d before electrophysiological recordings. Each oocyte was injected with 50–56 ng of either *SCN5A* cRNA alone or a combination of *SCN5A* and *Fgf12B/Fgf13VY* cRNAs at a 4:1 M ratio for coexpression.

Cut-open voltage-clamp recordings were performed at $19^\circ C$, maintained with a temperature controller (HCC-100A; Dagan Corporation), using a cut-open amplifier (CA-1B; Dagan Corporation), interfaced to a computer using an A/D converter (Digidata 1440; Molecular Devices) and the pClamp version 10 software (Molecular Devices). Data were collected using Clampex (Molecular Devices) and analyzed using Clampfit 10.7

(Molecular Devices). The internal recording solution was composed of 105 mM *N*-methyl-D-glucamine (NMDG), 10 mM 2-(*N*-Morpholino)ethanesulfonic acid (MES) sodium salt (Na-MES), 20 mM HEPES, and 2 mM EGTA, at a pH level of 7.4, and the external recording solution contained 25 mM NMDG, 90 mM Na-MES, 20 mM HEPES, and 2 mM $Ca-MES_2$, at a pH level of 7.4.

For VCF, oocytes were labeled for 30 min on ice with 10 μ mol/liter of methanethiosulfonate-carboxytetramethylrhodamine (MTS-TAMRA; Santa Cruz Biotechnology) in a depolarizing solution composed of 110 mM KCl, 1.5 mM $MgCl_2$, 0.8 mM $CaCl_2$, 0.2 mM EDTA, and 10 mM HEPES at a pH of 7.1. Simultaneous recordings of ionic current and fluorescence emissions were collected on a custom rig as described previously (Rudokas et al., 2014; Varga et al., 2015; Zhu et al., 2017). After teal LED light illumination by the SPECTRA X (Lumencor), fluorescence emission was measured by a photodiode (PIN-040A; United Detector Technology) and a patch-clamp amplifier (Axopatch-200A; Molecular Devices).

Voltage-clamp records were analyzed with Clampfit (Molecular Devices) and Excel (Microsoft). Steady-state activation curves were generated from currents recorded during 100-ms voltage steps to various test potentials (-120 to 60 mV) from a HP of -120 mV. The calculated conductance (G) was normalized to the maximum conductance at 20 mV. For steady-state inactivation curves, cells were preconditioned at voltages ranging from -150 to 20 mV for 200 ms and the channel availability at -20 mV was then determined. The normalized conductance-voltage ($G-V$) curves were fitted with a Boltzmann equation (Eq. 1). The time constants describing the fast inactivation kinetics of the currents were calculated by fitting the peak current decay to a sum of two exponentials function (Eq. 2).

Recovery from inactivation was determined by a double-pulse protocol with varying recovery durations between two pulses. The first depolarizing pulse was applied at -20 mV for 200 ms to induce fast inactivation. The second pulse, applied at -20 mV for 20 ms, was used to test channel recovery. The recovery duration was measured from 1 to 1,000 ms, and the normalized recovery curve was fitted to a double exponential equation (Eq. 3).

Fluorescence signals were first low-pass filtered at 1 kHz and then corrected for photobleaching after baseline subtraction. A fluorescence trace obtained at -120 mV, the HP, was fitted as a model for calculating baseline traces with no change in fluorescence at other potentials. The voltage-dependence of the normalized steady-state fluorescence emission ($F-V$) curve was fitted to a Boltzmann equation (Eq. 4):

$$F(V) = 1/(1 + \exp[-(V - V_{1/2})/k]), \quad (4)$$

where $V_{1/2}$ is the half-activation voltage and k is the slope factor.

Electrophysiological data analyses

Electrophysiological data were analyzed using Clampfit (Molecular Devices) and Prism 9 (Graph Pad). The statistical significance of apparent differences between/among data sets was evaluated with Welch ANOVA, followed by Dunnett's post-hoc test. Comparisons between the two groups were done using the

unpaired Welch's *t* test. Pearson correlation analysis was used to determine correlation coefficients (*r*), together with the coefficients of determination (R^2). Multiple linear regression analysis was applied to test the relationship between parameters of different measurements.

Western blot analyses

Protein lysates were prepared from WT, *Fgf12KO*, *cFgf13KO*, and hFGF12B- + eGFP-expressing *cFgf13KO* ventricles and from *Fgf12KO* atria in 20 mM HEPES + 150 mM NaCl buffer with 0.5% CHAPS and a protease inhibitor tablet (Roche) using previously described methods (Marionneau et al., 2008). Lysates were fractionated by SDS-PAGE (4–15% gradient), transferred to polyvinylidene fluoride (PVDF) membranes (Biorad), and probed for: iFGF13 expression using a rabbit polyclonal anti-iFGF13 antibody (generous gift of Dr. Geoffrey Pitt, Weill Cornell Medical School); eGFP expression using a rabbit polyclonal anti-eGFP antibody (catalog number AB3080; Sigma-Aldrich); or iFGF12 expression using a rabbit polyclonal anti-iFGF12 antibody (catalog number SAB2700759; Sigma-Aldrich). Blots were also probed with a mouse monoclonal anti-tubulin (1:10,000; Abcam) antibody to verify equal protein loading of the gel lanes.

RNA preparation and quantitative RT-PCR analysis

Quantitative RT-PCR analyses were completed using previously described methods (Marionneau et al., 2008). Briefly, for the preparation and analyses of RNA, adult (9–10 wk) WT ($n = 6$), *cFgf13^{-/-}* ($n = 6$), and *Fgf12^{-/-}* ($n = 6$) animals were sacrificed by cervical dislocation under isoflurane anesthesia and the hearts were rapidly removed. LVs were dissected and snap-frozen in liquid nitrogen. After homogenization, total RNA was isolated using the TRIzol Reagent (Invitrogen), and DNase was treated with the RNeasy Fibrous Tissue Mini Kit (Qiagen). The concentration of total RNA in each sample was measured spectrophotometrically using a NanoDrop ND-1000 (NanoDrop Technologies). RNA quality was examined using gel electrophoresis, and genomic DNA contamination was assessed by PCR amplification of total RNA without prior cDNA synthesis; no genomic DNA was detected.

First-strand cDNA was synthesized from 2 μ g of total RNA using the High-Capacity cDNA Archive Kit (Applied Biosystems). The expression levels of the *Fgf13VY*, *Fgf13S(A)*, *Fgf13U(B)*, *Fgf12B*, *Fgf12A*, *Fgf11*, *Fgf14A*, and *Fgf14B* transcripts were determined by quantitative real-time RT-PCR using SYBR Green PCR Master Mix (Applied Biosystems). PCR reactions were performed on 10 ng of cDNA using sequence-specific primer pairs (Table S1 B) and the ABI PRISM 7900HT Sequence Detection System. The cycling conditions included a hot start at 95°C for 10 min, followed by 40 cycles at 95°C for 15 s, and 60°C for 1 min. All primer pairs were tested using mouse cDNA as the template, and templates giving 90–100% efficiency were chosen. In all cases, a single amplicon of the appropriate melting temperature or size was detected using the dissociation curve or gel electrophoresis. Data were collected with instrument spectral compensations using the Applied Biosystems SDS 2.2.2 software and analyzed using the comparative threshold cycle (C_T) relative quantification method (Schmittgen and Livak, 2008). The

hypoxanthine-guanine phosphoribosyl-transferase gene (HPRT) was used as an endogenous control to normalize the data (deKok et al., 2005). Individual sample measurements ($n = 6$) were averaged and $2\Delta^{CT}$ values for each gene, corresponding to the relative expression level of that gene compared with HPRT, were calculated and are reported here; all C_T values were <30 . Negative control experiments using RNA samples incubated without reverse transcriptase during cDNA synthesis showed no amplification.

Online supplemental material

Fig. S1 illustrates the generation and validation of cardiac-specific deletion of *Fgf13* in mice. Fig. S2 shows the measurement of *Fgf* transcripts expression in WT, *cFgf13KO*, and *Fgf12KO* adult mouse LVs. Fig. S3 shows the amplitudes/densities of I_{Na} in *cFgf13KO* and *Fgf12KO* mouse LV myocytes. Fig. S4 shows the time dependence of AAV9-mediated expression of iFGF12B and eGFP in adult mouse LV. Fig. S5 portrays results from the iFGF chimeras experiment switching the N-terminal domains between iFGF12B and iFGF13VY. Fig. S6 demonstrates the effects of multiple iFGF chimeras on the voltage dependence of VSD-IV activation. Fig. S7 illustrates additional correlation and linear regression analysis between the VSD-IV activation and I_{Na} gating kinetics. Table S1 lists primers used in screening *Fgf13 floxed* (*Fgf13^{fl/+}* and *Fgf13^{fl/fl}*) and *cFgf13KO* mice. Table S2 lists biexponential fits to the decay phases of I_{Na} recorded at various test potentials from LV myocytes isolated from WT, *cFgf13KO*, and *cFgf13KO* + iFGF12B mice. Table S3 lists biexponential fits to the decay phases of I_{Na} evoked at various test potentials from oocytes expressing $Na_v1.5$ alone or $Na_v1.5$ combined with iFGF12B or iFGF13VY. Table S4 lists properties of I_{Na} recorded from *Xenopus* oocytes expressing $Na_v1.5$ in combination with iFGF chimeras.

Results

Loss of *Fgf13* alters the properties of I_{Na} in adult mouse LV myocytes

To generate mice (*cFgf13KO*) with cardiac-specific deletion of *Fgf13*, we floxed the *Fgf13* locus, using CRISPR-Cas 9 gene editing technology, and crossed these mice with transgenic mice expressing Cre-recombinase driven by the cardiac-specific α -MHC promoter as described in Materials and methods (Fig. S1, A and B). The loss of the *Fgf13* transcript and the iFGF13 protein in the heart was confirmed by quantitative RT-PCR (Fig. S2) and Western blot analyses (Fig. S1 C, left; and Fig. S2). Whole-cell voltage-clamp recordings revealed that the waveforms and the densities of the voltage-gated I_{Na} in LV myocytes isolated from WT and cardiac-specific *Fgf13* deletion (*cFgf13KO*) mice are remarkably similar (Fig. 1 A). Quantitative analyses of peak I_{Na} densities revealed no significant differences in *Fgf13 floxed*, compared with WT (P values >0.10 at all voltages), or in *cFgf13KO*, compared with *Fgf13 floxed* or WT (P values >0.15 at all voltages; Fig. S3 A). Analysis of the voltage-dependences of steady-state activation and inactivation of I_{Na} in WT and *cFgf13KO* LV myocytes revealed a hyperpolarizing shift in the voltage at which half the channels are inactivated ($V_{1/2, inact}$),

Table 1. Properties of I_{Na} in LV myocytes isolated from various mouse lines^a

	WT	<i>Fgf13</i> floxed	<i>cFgf13KO</i>	<i>cFgf13KO</i> + <i>iFGF12B</i>	<i>Fgf12KO</i>
G-V activation (n)	(24 cells, 7 mice)	(15 cells, 6 mice)	(26 cells, 8 mice)	(19 cells, 4 mice)	(19 cells, 6 mice)
$V_{1/2, act}$ (mV)	-46.3 ± 0.6	-44.1 ± 1.0	-44.4 ± 0.6	-37.48 ± 0.9	-44.6 ± 0.8
P value ^b		0.45	0.28	<0.001 (***)	0.69
P value ^c			0.99	<0.001 (***)	0.99
P value ^d				<0.001 (***)	
k_{act}	3.6 ± 0.1	2.9 ± 0.2	4.0 ± 0.1	4.3 ± 0.1	3.7 ± 0.2
P value ^b		0.93	0.17	0.002 (**)	0.99
P-value ^c			0.99	0.73	0.99
P value ^d				0.51	
G-V inactivation (n)	(24 cells, 7 mice)	(15 cells, 6 mice)	(26 cells, 8 mice)	(17 cells, 4 mice)	(19 cells, 6 mice)
$V_{1/2, inact}$ (mV)	-73.4 ± 1.0	-72.8 ± 1.3	-82.5 ± 0.8	-77.2 ± 0.5	-70.1 ± 1.0
P value ^b		0.99	<0.001 (***)	0.028 (*)	0.26
P value ^c			<0.001 (***)	0.05 (*)	0.67
P value ^d				<0.001 (***)	
k_{inact}	7.2 ± 0.1	7.1 ± 0.1	6.7 ± 0.2	6.9 ± 0.1	7.2 ± 0.1
P value ^b		0.99	0.10	0.23	0.99
P value ^c			0.62	0.92	0.99
P value ^d				0.19	
Inactivation recovery (n)	(9 cells, 2 mice)		(9 cells, 2 mice)	(9 cells, 2 mice)	
$T_{R,1}$ (ms)	8.2 ± 1.3		6.3 ± 0.9	4.0 ± 0.6	
P value ^b			0.38	0.015 (**)	
P value ^d				0.04 (*)	
$T_{R,2}$ (ms) ^e	85.4 ± 18.1		58.9 ± 8.4	28.2 ± 2.8	

^aValues are means ± SEM; n = number of biological replicates (cells and mice).

^bP values are obtained from a comparison to recordings in WT LV myocytes (see Materials and methods). Significant differences are designated as *, **, and *** for P values <0.05, 0.01, and 0.001, respectively.

^cP values are obtained from a comparison to recordings in *Fgf13* floxed LV myocytes. Significant differences are designated as *, **, and *** for P values <0.05, 0.01, and 0.001, respectively.

^dP values are obtained from a comparison to recordings in *cFgf13KO* LV myocytes. Significant differences are designated as *, **, and *** for P values <0.05, 0.01, and 0.001, respectively.

^eRecovery time constant for the slower component contributes very little. A comparison is thus omitted.

whereas the voltages at which half the channels are activated ($V_{1/2, act}$) in WT and *cFgf13KO* LV myocytes are indistinguishable (Fig. 1 B and Table 1). The finding that steady-state inactivation of I_{Na} is selectively affected in *cFgf13KO* LV myocytes is consistent with previous studies with acute, shRNA-mediated, knockdown of *Fgf13* or the targeted deletion of *Fgf13* (Wang et al., 2011a; Park et al., 2016; Wang et al., 2017; Park et al., 2020).

Additional experiments revealed that the kinetics of I_{Na} recovery from inactivation, determined from measurements of the normalized peak I_{Na} amplitudes as a function of the recovery interval as described in Materials and methods, are similar in WT and *cFgf13KO* LV myocytes (Fig. 1 C and Table 1). The records in Fig. 1 A and the overlay of I_{Na} recordings evoked at -20 mV (Fig. 1 D, inset), however, reveal that the conditional knockout of *Fgf13* accelerated peak I_{Na} decay. In WT LV myocytes, the decay phases of the currents were best fitted with a sum of two exponentials, providing the fast (T_f) and slow (T_s) time constants of

peak I_{Na} decay, corresponding to the fast and intermediate modes of open-state inactivation (Silva, 2014; Silva and Goldstein, 2013a; Silva and Goldstein, 2013b). Analyses of I_{Na} in *cFgf13KO* LV myocytes, however, revealed that the decay phases of the currents in many (13 of 26) *cFgf13KO* cells were not well-fitted by the sum of two exponentials. Rather, the decay phases of I_{Na} in these cells were well-described by single exponential with T values similar to the fast component (T_f) determined in WT cells. For all cells in which two exponentials were required, T_f and T_s were similar to the values determined in WT LV myocytes (Fig. 1 D and Table S2), although the relative amplitude of the slow component of I_{Na} decay (%Aslow) in the (13) *cFgf13KO* LV myocytes with two decay components was much lower than in WT LV myocytes (Fig. 1 E and Table S2). The apparent acceleration of I_{Na} decay in *cFgf13KO* LV myocytes (Fig. 1, A and D, inset), therefore, reflects a reduction (or, in many cells, elimination) of the slow component of current decay.

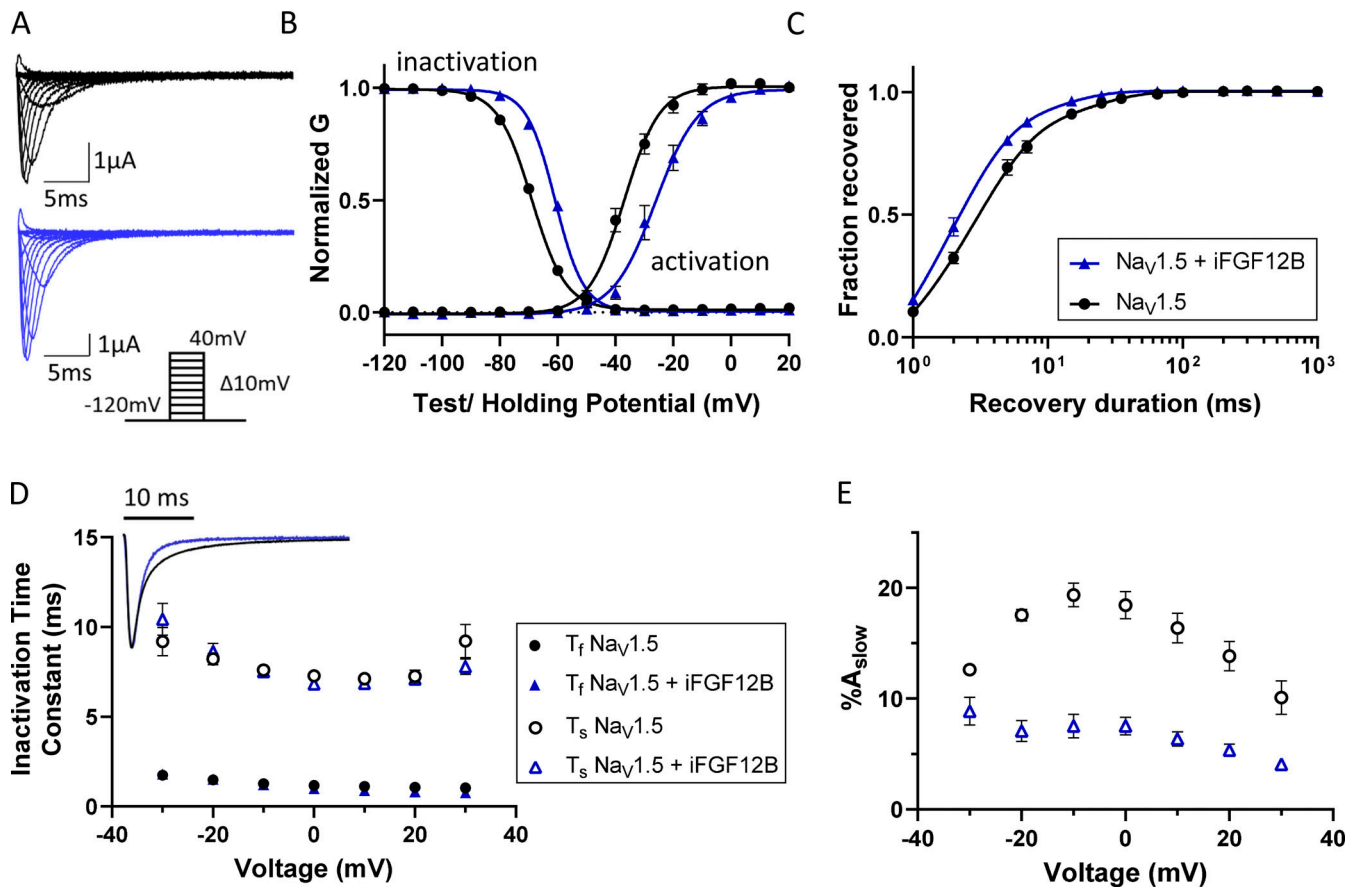


Figure 3. Coexpression of iFGF12B modulates the time- and voltage-dependent properties of $Na_v1.5$ -encoded currents in *Xenopus* oocytes. (A) Representative human $Na_v1.5$ -encoded (I_{Na}) waveforms recorded from *Xenopus* oocytes expressing $Na_v1.5$ alone (black) or together with iFGF12B (blue); the voltage-clamp protocol is illustrated below the current records. (B) The mean \pm SEM normalized conductance-versus-voltage plots reveal marked depolarizing shifts in the voltage-dependencies of activation and inactivation of the currents with iFGF12B coexpression (blue), relative to $Na_v1.5$ expressed alone (black; P values are 0.012 and <0.001 , respectively; Table 2). (C) The rate of I_{Na} recovery from inactivation is also accelerated with iFGF12B coexpression (P value = 0.04; Table 2). (D and E) Inset: Overlaying representative I_{Na} waveforms, recorded on membrane depolarizations to -20 mV, illustrates the difference in the decay phases of the currents recorded from *Xenopus* oocytes expressing $Na_v1.5$ alone (black) or $Na_v1.5$ with iFGF12B (blue). Analyses of the decay phases of the currents revealed that the time constants of the fast and slow components of I_{Na} decay (T_f and T_s , respectively; D) are indistinguishable in the absence and the presence of iFGF12B, whereas the fractional amplitude of the slow component of current decay ($\%A_{slow}$; E) was reduced markedly with iFGF12B coexpression at all test potentials (see values in Table S3).

Expression of iFGF13VY, therefore, reduces the fast component of I_{Na} decay.

Additional experiments revealed that the amplitudes and properties of I_{Na} recorded from LV myocytes isolated from *Fgf2*KO (Fig. S3, B and C) mice were indistinguishable from the currents in WT cells (Table 1), consistent with the negligible expression of *Fgf2* in adult mouse ventricles (Fig. S2).

Distinct effects of iFGF12B expression on I_{Na} in *cFgf13KO* LV myocytes

To examine the effects of iFGF12B on native I_{Na} , we generated an iFGF12B-expressing AAV9 and delivered this virus, mixed at a 1:1 ratio with eGFP-expressing AAV9, into *cFgf13KO* mice by retro-orbital sinus injection (see Materials and methods and Fig. S4). Representative recordings of I_{Na} from control *cFgf13KO* LV myocytes and an iFGF12B- + eGFP-expressing *cFgf13KO* LV myocytes are presented in Fig. 2 A. As illustrated in Fig. 2 B, the expression of iFGF12B shifted the voltage-dependence of I_{Na} inactivation in

the depolarizing direction relative to the results in *cFgf13KO* myocytes, i.e., back toward the WT G-V plot (Table 1). In addition, however, iFGF12B expression shifted the activation curve for I_{Na} , also in the depolarizing direction relative to the G-V curve for *cFgf13KO* and WT (Fig. 2 B) LV myocytes. The addition of iFGF12B did not alter the amplitudes of I_{Na} when compared to I_{Na} recorded from *cFgf13KO* (or WT) myocytes (Fig. 2 A). The addition of iFGF12B also accelerated the kinetics of I_{Na} recovery from inactivation, relative to the data in *cFgf13KO* myocytes (Fig. 2 C and Table 1). Analyses of the waveforms of the currents in *cFgf13KO* LV myocytes expressing iFGF12B, however, revealed that, similar to *cFgf13KO* LV myocytes, the decay phases of the currents in many (13 of 19) cells were best described by single exponentials characterized by T values similar to T_f measured in WT and *cFgf13KO* LV myocytes (Table S2). For the remaining (6 of 19) *cFgf13KO* LV myocytes expressing iFGF12B, I_{Na} was well-described by the sum of two exponentials with T_f and T_s values and $\%A_{slow}$ similar to those measured in *cFgf13KO* LV myocytes

Table 2. **Properties of I_{Na} determined in *Xenopus* oocytes expressing $Na_v1.5$ alone or in combination with iFGF12B or iFGF13VY^a**

	$Na_v1.5$	$Na_v1.5$ + iFGF12B	$Na_v1.5$ + iFGF13VY
G-V activation (n)	(5)	(6)	(6)
$V_{1/2, act}$ (mV)	-37.0 ± 0.6	-26.2 ± 2.2	-32.3 ± 3.1
P value ^b		0.006 (**)	0.33
k_{act}	6.1 ± 0.3	6.6 ± 0.4	5.5 ± 0.5
P value ^b		0.44	0.60
G-V inactivation (n)	(9)	(7)	(6)
$V_{1/2, inact}$ (mV)	-69.0 ± 0.5	-60.9 ± 0.4	-54.5 ± 1.8
P value ^b		<0.001 (***)	<0.001 (***)
k_{inact}	5.8 ± 0.3	4.9 ± 0.3	4.7 ± 0.4
P value ^b		0.06	0.09
Inactivation recovery (n)	(8)	(5)	(5)
$T_{R,1}$ (ms)	2.5 ± 0.2	1.9 ± 0.3	1.3 ± 0.1
P value ^b		0.04 (*)	<0.001 (***)
$T_{R,2}$ (ms) ^c	15.8 ± 1.4	12.5 ± 1.3	8.5 ± 1.3

^aValues are means \pm SEM; n = number of biological replicates (cells).

^bP values are obtained from a comparison to recordings from oocytes expressing $Na_v1.5$ alone (see Materials and methods). Significant differences are designated as *, **, and *** for P values <0.05, 0.01, and 0.001, respectively.

^cRecovery time constant for the slower component contributes very little. A comparison is thus omitted.

(Fig. 2, D and E; and Table S2). In contrast with iFGF13VY, therefore, iFGF12B does not measurably affect the fast or the slow component of decay of mouse ventricular I_{Na} .

The results presented above demonstrate that iFGF13VY and iFGF12B have distinct effects on the time- and voltage-dependent properties of native (mouse) myocardial I_{Na} . To explore the molecular mechanisms underlying these differences, we turned to a heterologous expression system (*Xenopus* oocytes) and obtained voltage-clamp current and VCF recordings from oocytes expressing $Na_v1.5$ alone or in combination with iFGF12B or iFGF13VY.

iFGF12B regulates $Na_v1.5$ kinetics via the modulation of VSD-IV activation

In subsequent experiments, $Na_v1.5$ -encoded currents were recorded from *Xenopus* oocytes expressing $Na_v1.5$ alone or $Na_v1.5$ combined with iFGF12B (Fig. 3 A). In comparison to $Na_v1.5$ alone, iFGF12B coexpression shifted the steady-state activation and inactivation curves in the depolarizing direction (Fig. 3 B and Table 2). In the presence of iFGF12B, therefore, $Na_v1.5$ channels begin to open at more depolarized membrane potentials. The rate of recovery of I_{Na} from inactivation was also faster in the presence of iFGF12B (Fig. 3 C and Table 2).

Superimposing recordings of I_{Na} evoked by a -20 -mV voltage step from oocytes expressing $Na_v1.5$ alone or $Na_v1.5$ with

iFGF12B revealed that current decay was accelerated with iFGF12B coexpression (Fig. 3 D, inset). Analyses of the kinetics of peak I_{Na} decay revealed that the data were best fit to the sum of two exponentials, and the measured time constants (T_f and T_s) were similar for the currents produced by $Na_v1.5$ alone and $Na_v1.5$ combined with iFGF12B (Fig. 3 D and Table S3). The fractional amplitudes of the slower component of inactivation (% A_{slow}), however, were markedly reduced in the presence of iFGF12B (Fig. 3 E and Table S3). iFGF12B, therefore, enhanced the faster component of inactivation of heterologously expressed (human) $Na_v1.5$.

Next, we employed VCF to probe the molecular mechanism(s) contributing to iFGF12B modulation of $Na_v1.5$ channel gating (Mannuzzo et al., 1996; Stefani and Bezanilla, 1998; Gandhi and Olcese, 2008; Rudokas et al., 2014). A cysteine mutation was introduced into the extracellular linker S3-S4 in each VSD for fluorophore (MTS-TAMRA) tagging (Varga et al., 2015; Zhu et al., 2016). The movement of S4 upon membrane depolarization can then be detected by a change in fluorescence emission, reflecting an altered surrounding environment (Varga et al., 2015; Zhu et al., 2016). To improve sensitivity, a cysteine mutation was created in the background of WT-LFS (large fluorescence signal) bearing Y1977A-C373Y mutations that ablate a ubiquitination site and prevent non-specific labeling (Varga et al., 2015). Previous work showed that the LFS mutations do not substantially affect Na_v channel activation or inactivation kinetics (Varga et al., 2015). Plotting changes in the fluorescence signals as a function of voltage (i.e., F versus V curves) for each VSD allows estimation of the conformational changes that occur during VSD activation.

As illustrated in Fig. 4, coexpression of iFGF12B caused no changes in the half-maximal voltages ($V_{1/2}$) of VSD-I, VSD-II, or VSD-III F-V curves compared with $Na_v1.5$ expressed alone. For VSD-III, however, we observed a change at potentials greater than -50 mV. Multiple lines of evidence suggest that VSD-III can activate in two discrete steps (Chanda and Bezanilla, 2002; Hsu et al., 2017; Zhu et al., 2017). iFGF12B did not affect the initial activation at very hyperpolarized potentials. However, the second transition of VSD-III was modulated by iFGF12B, as seen by the deflection at higher potentials (Fig. 4). This second VSD-III activation has been proposed to regulate the open-state inactivation (Angsutrarux et al., 2021a).

iFGF12B coexpression induced marked changes in the F-V curve of VSD-IV F-V, specifically causing a hyperpolarizing shift in $V_{1/2}$ and a decrease in the slope factor (k ; Fig. 4 and Table 3). The alterations in the F-V curve in the presence of iFGF12B reflected the facilitated activation of VSD-IV and its accelerated outward transition, resulting in its fully activated conformation at less depolarized potentials. Together, these results suggest that the facilitation of VSD-IV activation underlies the observed effects of iFGF12B on the gating properties and kinetics of I_{Na} inactivation.

Distinct effects of iFGF13VY on $Na_v1.5$ gating and VSD activation

Next, we investigated the effect of iFGF13VY on $Na_v1.5$. Analysis of the ionic currents (Fig. 5 A) produced on the expression of

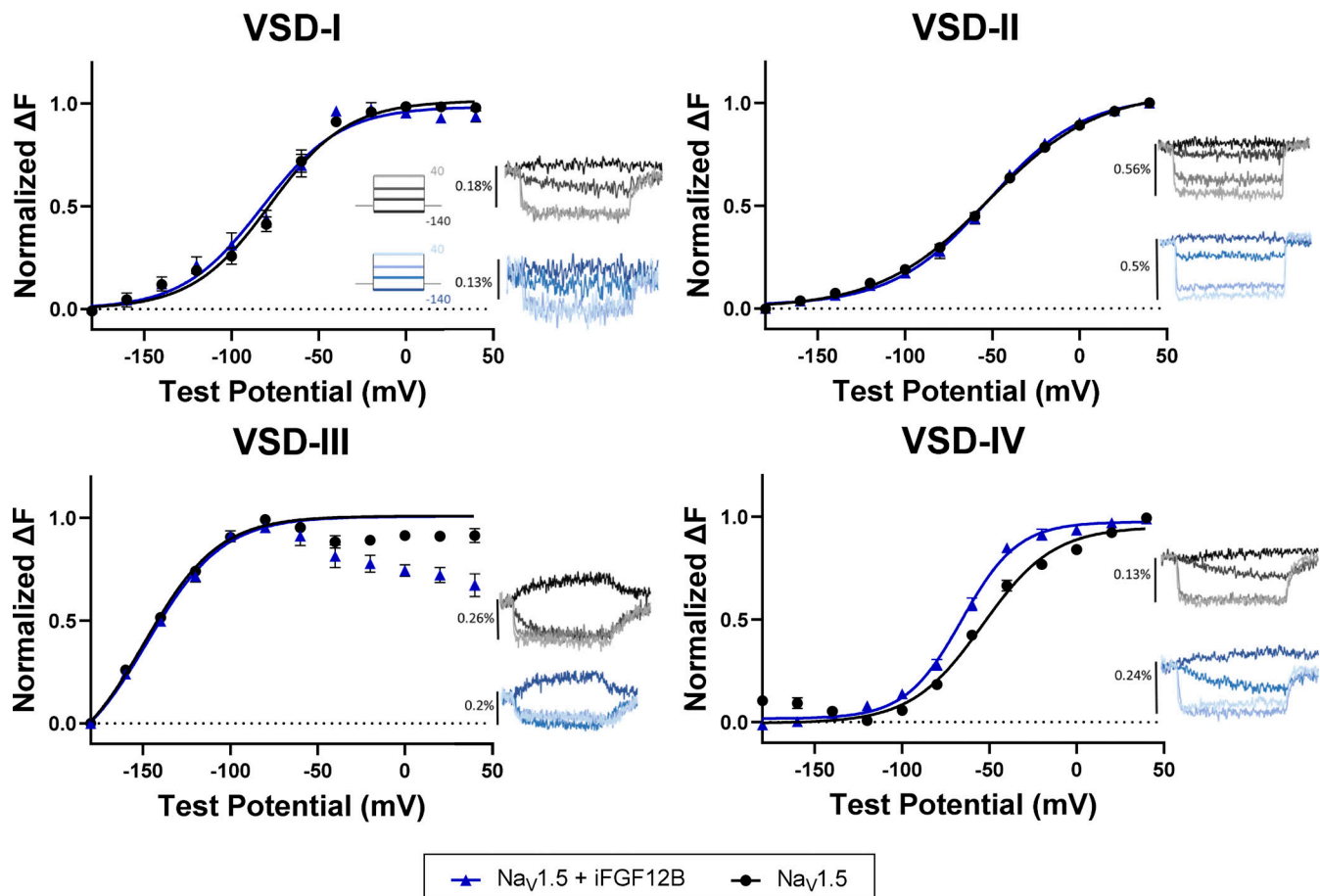


Figure 4. **iFGF12B regulates the activation of the voltage sensor in repeat IV of Na_v1.5.** VCF recordings were obtained as described in Materials and methods. Representative fluorescence signals recorded from *Xenopus* oocytes expressing Na_v1.5 alone (black) or with iFGF12B (blue) in response to 50-ms depolarizing voltage steps to -140, -80, -20, and 40 mV, are presented; only four fluorescence traces are shown for clarity. The mean \pm SEM normalized steady-state fluorescence signals were plotted and fitted with a single Boltzmann function (solid lines). Coexpression of iFGF12B induced a hyperpolarizing shift in the VSD-IV F-V curve (P value <0.001, Table 3), but caused no change in the F-V curves of the other VSDs (see Table 3).

Na_v1.5 alone and Na_v1.5 coexpressed with iFGF13VY revealed a shift in the steady-state inactivation curve toward depolarizing potentials in the presence of iFGF13VY, with no effect on the voltage-dependence of current activation (Fig. 5 B and Table 2). The depolarizing shift in the $V_{1/2}$ for inactivation seen with iFGF13VY (Fig. 5 B and Table 2) was substantially larger than the shift seen with coexpression of iFGF12B (Fig. 3 B and Table 2). Recovery from inactivation was also facilitated by iFGF13VY (Fig. 5 C and Table 2). Compared to Na_v1.5 alone, we also found that iFGF13VY coexpression accelerates the apparent rate of current decay (Fig. 5 D, inset) by reducing %A_{slow} (Fig. 5 E), as T_f and T_s are unchanged in the presence of iFGF13VY (Fig. 5 D and Table S3).

Examination of the activation of the individual VSDs revealed marked effects of iFGF13VY on the F-V curves for VSD-I and VSD-IV (Fig. 6 and Table 3). The VSD-I F-V curve was shifted toward positive potentials with iFGF13VY coexpression (Fig. 6), an effect that is not observed with iFGF12B (Fig. 4). iFGF13VY coexpression also increases the steepness (slope) of the F-V curve for VSD-IV and results in a hyperpolarizing shift in the $V_{1/2}$. The modulatory effects of iFGF13VY on VSD-IV activation

(Fig. 6), therefore, are distinct from the effect of iFGF12B (Fig. 4). iFGF13VY markedly increased the slope of the F-V curve (reduced slope factor k), whereas iFGF12B shifted the $V_{1/2}$ in the hyperpolarizing direction.

iFGF chimeras to probe the distinct functional effects of iFGF12B and iFGF13VY on VSD-IV

Like other FGFs, the iFGFs consist of three main domains: the N-terminus, the β -trefoil core, and the C-terminus. The core domains of iFGF11–iFGF14 are highly homologous (Olsen et al., 2003). According to resolved crystal structures, the amino acid residues that mediate iFGF interaction with the C-termini of Na_v α subunits are in the core domain (Goetz et al., 2009; Wang et al., 2012; Musa et al., 2015; Hennessey et al., 2013). If the same residues are involved in the binding of iFGF12B and iFGF13VY to Na_v1.5, the distinct functional effects on Na_v channel gating must reflect interactions with other parts of these proteins which are distinct. Alignment of the iFGF12B and iFGF13VY proteins reveals the prominent difference in the N-termini of these two proteins (Fig. 7 A). Previous studies have shown that the unique N-terminal sequences of iFGF14 splice variant

Table 3. Parameters determined from Boltzmann fits to the voltage dependences of steady-state F-V curves for Na_v1.5 voltage sensor domains, VSD-I–VSD-IV^a

	Na _v 1.5	Na _v 1.5 + iFGF12B	Na _v 1.5 + iFGF13VY
VSD-I (n)	(4)	(3)	(4)
V _{1/2} (mV)	-75.2 ± 3.6	-77.6 ± 4.6	-50.1 ± 3.1
P value ^b		0.99	0.003 (**)
k	19.4 ± 0.9	21.2 ± 2.7	13.7 ± 1.2
P value ^b		0.97	0.008 (**)
VSD-II (n)	(5)	(4)	(5)
V _{1/2} (mV)	-51.6 ± 1.8	-53.1 ± 2.9	-53.4 ± 1.7
P value ^b		0.99	0.25
k	33.0 ± 4.9	27.4 ± 2.0	38.7 ± 0.9
P value ^b		0.84	0.50
VSD-III (n)	(10)	(8)	(6)
V _{1/2} (mV)	-149.7 ± 1.6	-145.6 ± 2.1	-153.4 ± 4.3
P value ^b		0.28	0.68
k	21.4 ± 0.8	20.6 ± 0.7	22.0 ± 2.0
P value ^b		0.71	0.95
VSD-IV (n)	(8)	(8)	(8)
V _{1/2} (mV)	-52.9 ± 2.0	-66.2 ± 2.3	-60.4 ± 1.3
P value ^b		0.001 (***)	0.02 (*)
k	20.5 ± 1.3	16.5 ± 1.2	9.4 ± 1.0
P value ^b		0.08	<0.001 (***)

^aValues are means ± SEM; n = number of biological replicates (cells).

^bP values are obtained from a comparison to recordings from oocytes expressing Na_v1.5 alone (see Materials and methods). Significant differences are designated as *, **, and *** for P values <0.05, 0.01, and 0.001, respectively.

N-termini result in distinct effects on Na_v channel gating (Lou et al., 2005; Laezza et al., 2009; Barbosa et al., 2017; Ali et al., 2018; Singh et al., 2020, 2021). Similarly, the differing N-terminal sequences of the five splice variants of iFGF13 (iFGF13S(A), iFGF13U(B), iFGF13V, iFGF13Y, and iFGF13VY) result in distinct regulatory effects on Na_v1.5 channel gating (Wang et al., 2017). In addition, it has been reported that the specific sequence of iFGF A variants, including iFGF12A, can inhibit the late sodium current, which is not observed with other splice variants, including iFGF12B (Chakouri et al., 2022). Together, these studies point to the significance of the iFGF N-termini in determining the specific modulatory effects of the different variants.

To determine whether the differences we observed in the effects of iFGF12B and iFGF13VY on Na_v1.5-encoded currents are the result of the distinct N-termini of these two proteins, we created two iFGF chimeras by swapping the N-terminal domains (NTD) of iFGF12B (aa1–4) and iFGF13VY (aa1–72), and iFGF12B/13 (12NTD–13Core–13CTD) and iFGF13VY/12 (13NTD–12Core–12CTD; Fig. S5 A). If the NTD was sufficient to produce an iFGF-specific effect, we would expect the shifts in the G-V and VSD-IV F-V

curves produced by the iFGF12B/13 and iFGF13VY/12 chimeras to resemble those produced by iFGF12B and iFGF13VY, respectively. These iFGF chimeras, however, produced modulatory effects on Na_v channels G-V and VSD-IV F-V curves that are different from the effects of iFGF12B and iFGF13VY (Fig. S5 B and Table S4), implying that the N-terminal sequence alone is not enough to confer the specificity of iFGF-mediated effects. Therefore, we generated additional chimeras switching (1) the C-termini or (2) both the N- and C-termini of iFGF12B and iFGF13VY. Remarkably, neither of these chimera pairs replicated the modulation of the VSD-IV F-V curves produced by iFGF12B and iFGF13VY (Fig. S6 and Table S4), suggesting that all iFGF domains contribute to VSD-IV regulation.

Activation of VSD-IV was previously shown to facilitate Na_v channel fast inactivation (Chahine et al., 1994; Horn et al., 2000; Chanda and Bezanilla, 2002; Hsu et al., 2017). In addition, charge neutralization mutations in the S4 segment of VSD-IV caused a shift in the V_{1/2} of inactivation of Na_v1.5 currents (Capes et al., 2013). To explore the relationships between VSD-IV regulation and Na_v1.5 gating kinetics, we investigated possible correlations between/among the measured voltage-dependences of I_{Na} activation and inactivation, I_{Na} decay kinetics, and VSD-IV F-V curves for Na_v1.5 coexpressed with each of the iFGF chimeras (Table S4). Surprisingly, the iFGF and iFGF chimera data showed no correlation between the V_{1/2} values determined for steady-state inactivation of I_{Na} (V_{1/2, inact}) and the VSD-IV F-V curves, yielding a Pearson's correlation coefficient (r) equal to 0.23 and an R² of 0.054 (Fig. S7 A), and only modest correlation with the slope (k) values (r = 0.62, R² = 0.4; Fig. S7 C). Similarly, no correlation was found between the voltage-dependences of I_{Na} activation (V_{1/2, act}) and the VSD-IV F-V curves (for V_{1/2}: r = 0.005, R² = 3 × 10⁻⁵, for k: r = -0.34, R² = 0.12; Fig. S7, B and D).

These analyses, however, did reveal that the slope (k values) of the VSD-IV F-V curves correlated with the parameters describing I_{Na} decay, specifically with the slow inactivation time constants (τ_s) and the fractional amplitudes of the slow component of inactivation (%A_{slow}). As illustrated for I_{Na} evoked at 0 mV, the r and R² values between VSD-IV k values and the τ_s were 0.79 and 0.63 (Fig. 7 B). Similarly, the calculated r and R² values for the correlation between the measured %A_{slow} and VSD-IV k values were 0.76 and 0.59, respectively (Fig. 7 C). No correlations, however, were established between the V_{1/2} values of the VSD-IV F-V curves and neither the τ_{slow} nor the %A_{slow} of I_{Na} (for τ_{slow}: r = 0.53, R² = 0.29, for %A_{slow}: r = 0.06, R² = 0.004; Fig. S7, E and F).

Combining the two parameters derived from the VSD-IV F-V curves (i.e., V_{1/2} and k values) predicts the %A_{slow} with higher accuracy than achieved with the V_{1/2, inact}. The R² values between the predicted and actual values for %A_{slow} and the V_{1/2, inact} were 0.72 and 0.58, respectively (Fig. 7 D and Fig. S7 G). Together, these results suggest that the slope of VSD-IV F-V curve is a strong determinant of the slower component of Na_v channel inactivation. We also found that a steeper VSD-IV F-V curve, corresponding to the earlier completion of VSD-IV activation at more hyperpolarized potentials, contributes to a reduction in the relative amplitude of the slower component of inactivation. The absence of correlation between the V_{1/2, inact}

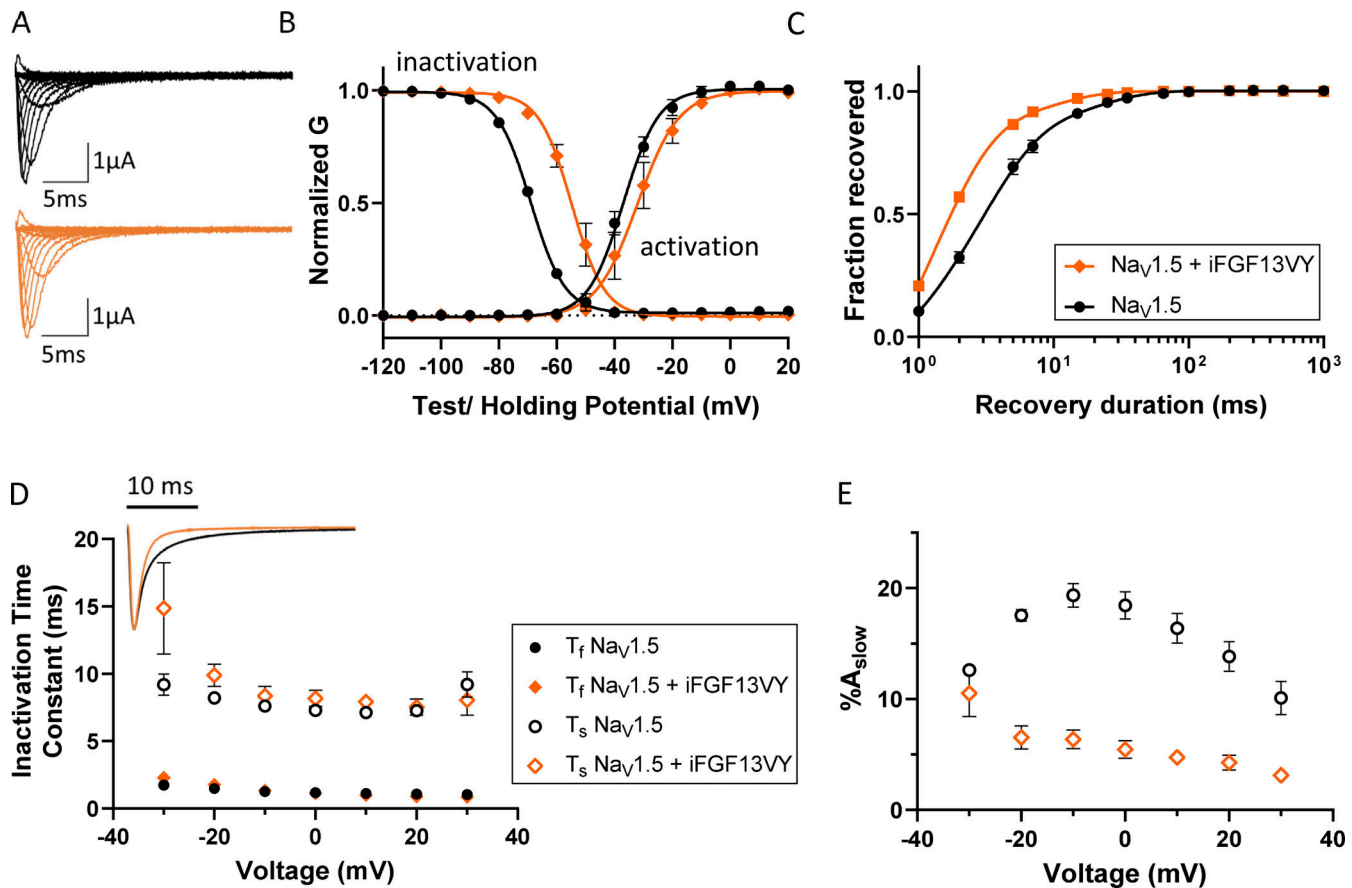


Figure 5. **Coexpression of iFGF13VY affects the voltage dependence of steady-state inactivation and the inactivation kinetics of $Na_v1.5$ -encoded currents in *Xenopus* oocytes.** (A) Representative I_{Na} waveforms recorded from *Xenopus* oocytes expressing $Na_v1.5$ alone (black) or with iFGF13VY (orange); the voltage-clamp protocol is illustrated below the current records. (B) The mean \pm SEM conductance versus voltage plots reveal marked depolarizing shifts in the voltage dependence of inactivation with iFGF13VY coexpression compared with $Na_v1.5$ expressed alone (P value <0.001 ; Table 2). The voltage dependence of I_{Na} activation, however, is not affected by iFGF13VY (P value = 0.3; Table 2). (C and D) Coexpression of iFGF13VY accelerated I_{Na} recovery from inactivation (C; P value <0.001 ; Table 2) and overlay of representative I_{Na} waveforms (D, inset), evoked at -20 mV, illustrates the difference in the decay phases of I_{Na} in recordings from *Xenopus* oocytes expressing $Na_v1.5$ without (black) and with (orange) iFGF13VY. (E) Analyses of the decay phases of the currents revealed that the time constants, T_f and T_s , of the fast and slow components of I_{Na} decay, respectively, (D) are indistinguishable for the currents in the absence and presence of iFGF13VY, whereas the fractional amplitude of the slow component of current decay ($\%A_{slow}$; E) was reduced markedly with iFGF13VY coexpression at all test potentials (see values in Table S3).

and the $V_{1/2}$ of VSD-IV F-V curve hints that at least one additional element is involved in iFGF modulation of the voltage-dependence of steady-state inactivation of $Na_v1.5$ currents.

Discussion

In this study, we demonstrate that the differential regulation of the time- and voltage-dependent properties of $Na_v1.5$ -encoded currents by iFGF12B and iFGF13VY reflects distinct effects on VSD-IV activation. Although previous studies have reported the importance of the iFGF N-terminal domain in the isoform-specific modulation of I_{Na} gating (Lou et al, 2005; Laezza et al, 2009; Yang et al, 2016; Barbosa et al, 2017; Ali et al, 2018; Singh et al, 2020, 2021; Chakouri et al, 2022), our results show that switching the N-termini of iFGF12B and iFGF13VY is not sufficient to confer the iFGF-specific modulation of $Na_v1.5$ channel gating and VSD-IV activation. Rather, our results indicate that all regions of the iFGF proteins (i.e., the N-terminal, core, and

C-terminal domains) contribute to determining iFGF-specific effects on I_{Na} gating and VSD-IV activation.

Physiological relevance

In native mouse cardiomyocytes, we observed a change in the voltage dependence of steady-state inactivation of I_{Na} with the deletion of iFGF13. This alteration results in decreased numbers of channels available to activate and conduct I_{Na} . The expression of iFGF12B in *cFgf13KO* ventricular myocytes rescues Na_v channel steady-state availability, revealing roles for the iFGF proteins in regulating cardiac myocyte excitability. Patients carrying mutations on the binding interface of iFGF12B and $Na_v1.5$ exhibit phenotypes associated with Brugada (Hennessey et al, 2013) and long-QT type 3 syndrome (Wang et al, 2012). In addition, a missense mutation in *Fgf12* was shown to increase arrhythmia susceptibility in mice (Veliskova et al, 2021). The expression of iFGF12B also exerts an additional effect on Na_v channel steady-state activation. The shift in voltage dependence

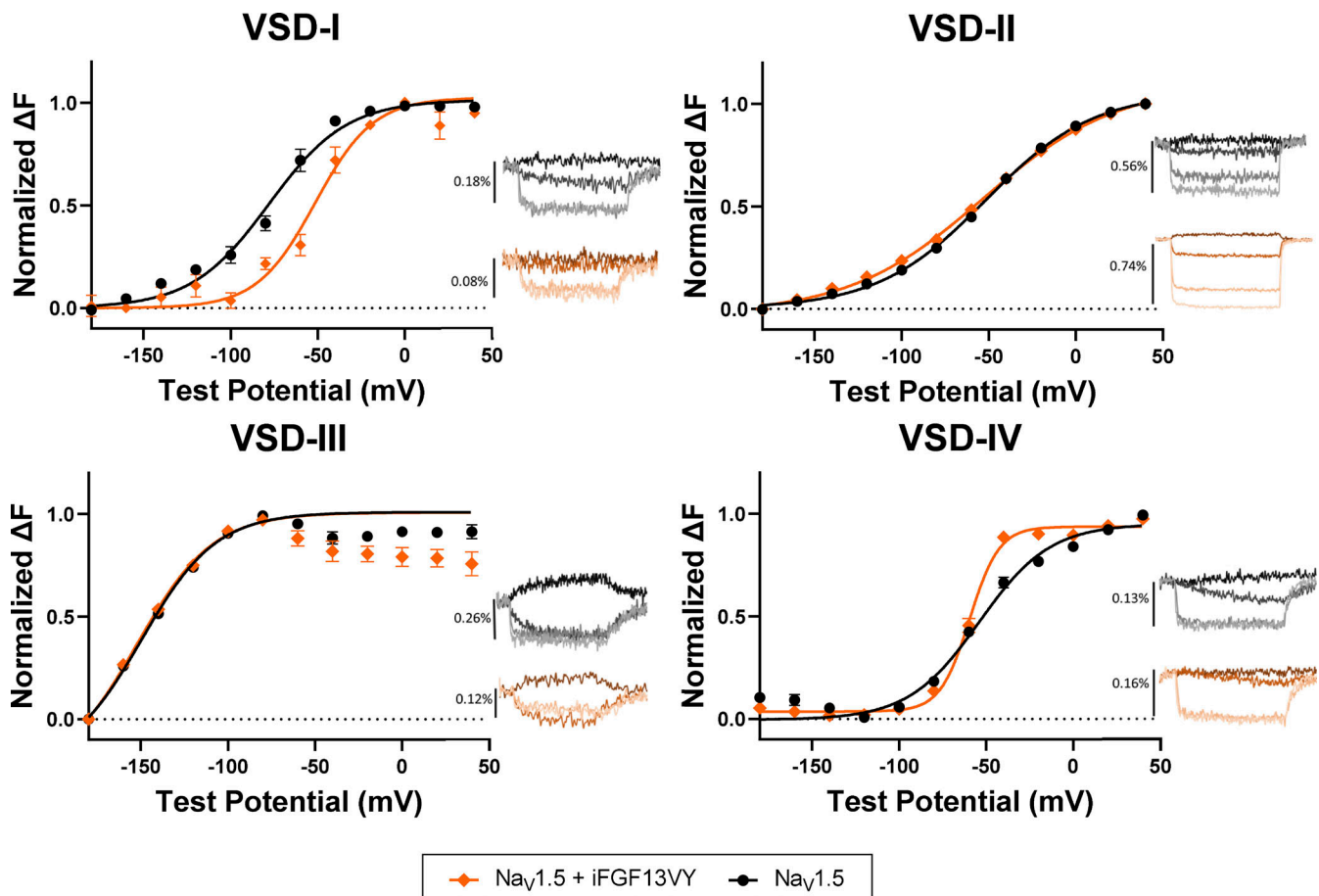


Figure 6. **Distinct modulation of $\text{Na}_V1.5$ voltage sensor conformations with iFGF13VY coexpression.** The F-V curves for all four VSDs of $\text{Na}_V1.5$ recorded from *Xenopus* oocytes expressing $\text{Na}_V1.5$ alone (black) or with iFGF13VY (orange) show that iFGF13VY affects the voltage-dependences of activation of VSD-I and VSD-IV. For VSD-I, iFGF13VY coexpression shifts the F-V curve toward depolarizing potentials (P value = 0.002; Table 3). For VSD-IV, the F-V curves show that iFGF13VY results in a steeper slope and a small shift toward more hyperpolarized membrane potentials relative to $\text{Na}_V1.5$ expressed alone (P values are 0.022 and <0.001, respectively; Table 3). The effect on the VSD-IV F-V curve with iFGF13VY coexpression is distinct from that observed with iFGF12B coexpression (compare with Fig. 4).

of I_{Na} activation toward more positive potentials with iFGF12B means that larger depolarizations are required to activate the channels and, therefore, to reach the threshold for triggering APs. This effect will lead to a longer refractory period, where myocytes cannot be activated and could suppress arrhythmic activity.

Previous studies of *Fgf13* knockdown or knockout in mice myocytes reported a reduction in the peak I_{Na} density (Wang et al., 2011a; Park et al., 2016; Wang et al., 2017). Here, however, we did not observe any significant reduction in the I_{Na} density with cardiac-specific iFGF13 knockout or with the addition of iFGF12B in *cFgf13KO* ventricles. These differences may reflect the mouse strain or knockout techniques employed or the I_{Na} recording conditions used in the previous versus the present studies. Interestingly, Park and colleagues reported a reduction in peak I_{Na} density in mouse ventricular myocytes lacking iFGF13 at 30°C but not at 25°C (Park et al., 2016). Whether iFGF12B and/or iFGF13VY directly affect cardiac $\text{Na}_V1.5$ trafficking and membrane localization, as demonstrated for iFGFs in some neuronal cells (Laezza et al., 2009), requires further study.

Comparing iFGF regulation of $\text{Na}_V1.5$ in myocytes and oocytes

The regulation of VSD-IV activation is evident not only with iFGFs but also with other Na_V channel accessory proteins including the β subunits. Past studies showed that both the $\text{Na}_V\beta1$ and $\text{Na}_V\beta3$ subunits induce depolarizing shifts in VSD-IV activation, i.e., effects opposite iFGFs-mediated effects (Zhu et al., 2017, 2021). The presence of $\text{Na}_V\beta$ subunits and other Na_V channel accessory subunits in mouse myocytes, therefore, could affect iFGF-mediated changes in I_{Na} decay kinetics, accounting for observed differences in inactivation kinetics compared with the results observed in the *Xenopus* oocyte expression systems. In addition, the binding of Ca^{2+} /calmodulin (CaM) on the Na_V C-terminus is in the same vicinity as iFGF binding and might influence the function of iFGF, similar to how iFGF enhances the CaM function in $\text{Na}_V1.5$ variants of reduced CaM binding affinity (Gade et al., 2020; Abrams et al., 2020). Different levels of Ca^{2+} /calmodulin could thus contribute to system-specific effects of iFGF. Finally, posttranslational modification, such as phosphorylation on the $\text{Na}_V1.5$ C-terminus, that occurs in mammalian cells, but not in *Xenopus* oocytes, can also affect the binding of iFGFs (Burel et al., 2017; Iqbal and Lemmens-Gruber, 2019;

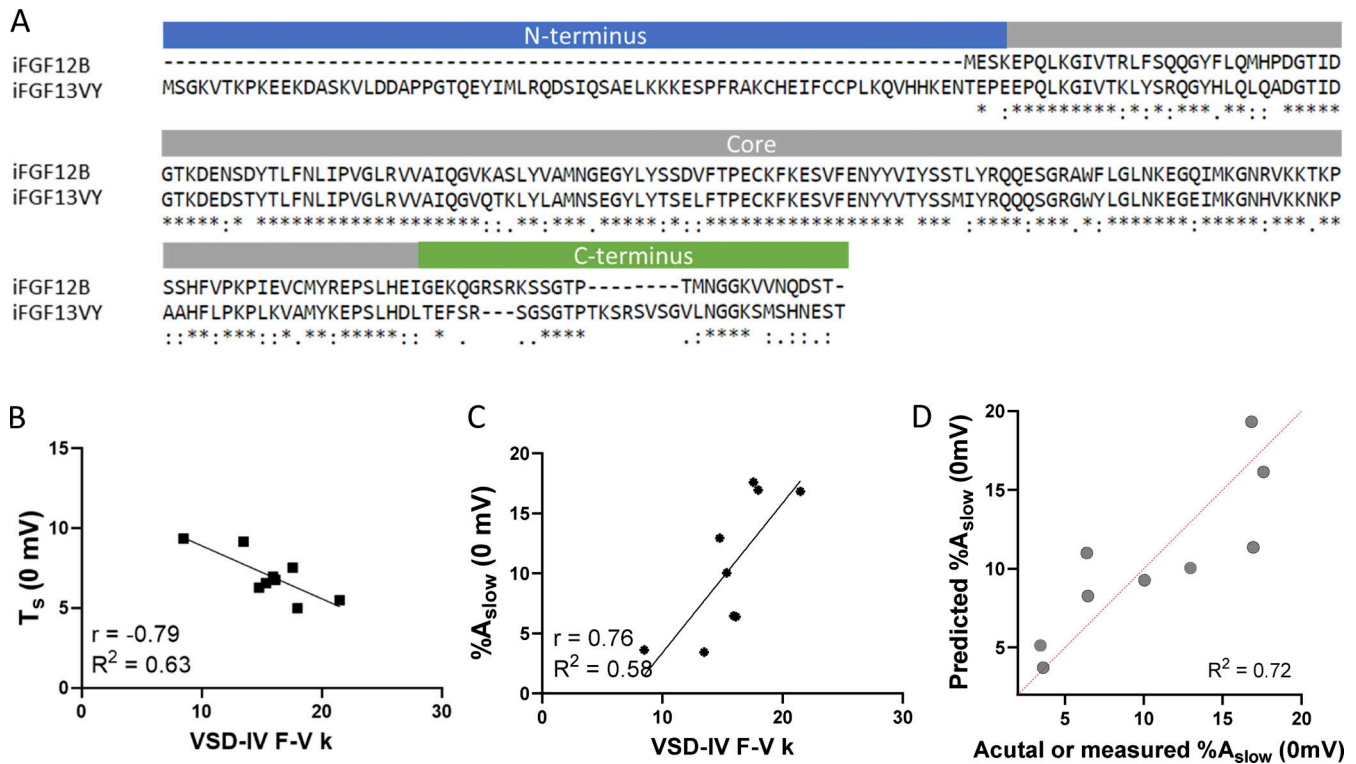


Figure 7. Analysis of iFGF12B, iFGF13VY, and iFGF12B/13VY chimeras reveals a strong correlation between the slopes of the VSD-IV F-V curves and the slow component of I_{Na} inactivation. (A) Alignment of the iFGF12B and iFGF13VY sequences highlights the prominent difference in N-termini. (B–D) Several iFGF12B/13VY chimeras were constructed by swapping the N-termini, C-termini, and both C- and N-termini domains. Each chimera was coexpressed with $Na_v1.5$, and effects on the time- and voltage-dependent properties of I_{Na} and VSD-IV activation were determined. Correlation and linear regression analyses were performed on these results obtained from iFGF chimeras, iFGF12B, and iFGF13VY. (B and C) The analyses revealed that the slow time constants of I_{Na} decay (T_s ; B) and the fractional amplitudes of the slow component ($\%A_{slow}$; C), determined for currents evoked at 0 mV, are both strongly (negatively [B] or positively [C]) correlated with the VSD-IV F-V k values. (D) The k and $V_{1/2}$ values, determined from the VSD-IV F-V curves, can be used to predict $\%A_{slow}$.

Lorenzini et al., 2021). The synergistic effects of multiple regulatory proteins and posttranslational channel modifications suggest that VSD-IV may act as a signaling hub where the regulation by many different Na_v channel complex components is integrated to determine inactivation kinetics. In addition, other Na_v α subunits, such as $Na_v1.6$, might be present in native mouse cardiomyocytes (Maier et al, 2004; Lopez-Santiago et al, 2007), producing I_{Na} with different gating properties and differentially affected by iFGF coexpression.

Contribution of different iFGF domains to $Na_v1.5$ regulation

The structures of the iFGF13/iFGF12 proteins in complex with the $Na_v1.5$ C-terminus reveal that the common iFGF core domain is critical for binding (Wang et al., 2012; Wang et al., 2014). In addition, the folding of the core domain is nearly identical in iFGF13 (PDB accession nos. 3HBW [Goetz et al., 2009] and 4DCK [Wang et al., 2012]) and iFGF12 (PDB accession nos. 1QIU [Goetz et al., 2009] and 4JQO [Wang et al., 2014]). It should also be noted that the iFGF N- and C-terminal domains are omitted from all of these structures. Both ends of the core domain structures, where the N- and C-terminal domains are located, however, are in the vicinity of the iFGF- $Na_v1.5$ interaction sites. The N- and C-terminal domains of the iFGFs, therefore, might be expected to also interact with other parts of the Na_v α subunit or assembled $Na_v1.5$ channel and influence channel/current

properties. Consistent with this hypothesis, it has previously been reported that mutation of a single proline residue in iFGF12 outside the iFGF- Na_v C-terminus binding interface altered the (iFGF- Na_v C-terminus) binding affinity (Wang et al., 2011b). Similar functional effects were observed when the corresponding proline residue in iFGF13 was modified. These observations led the authors of this study to suggest that the iFGFs may contain multiple Na_v α subunit interaction sites, each contributing to the specific modulatory effects of the iFGF on different Na_v α subunits and, therefore, on different Na_v channels (Wang et al., 2011b). It has also been demonstrated that the perturbation of iFGF binding sites at two distinct interfaces, for example, using (two) peptides mimicking different sequences of iFGF14, led to differential modulation of $Na_v1.6$ -encoded channel gating (Ali et al, 2018; Singh et al, 2021). The differential effects of the various iFGF proteins on Na_v channels/currents encoded by different Na_v α subunits is thus likely the result of multiple and variable interactions, involving the diverse iFGF N- and C-termini, as well as the canonical binding interface, and resulting in distinct functional effects on VSD-IV dynamics and Na_v channel gating.

Analyses of electrophysiological data obtained from iFGF12B/13VY chimeras coexpressed with $Na_v1.5$ revealed a strong correlation between the slope(s) of the VSD-IV activation curve(s) and the kinetics of I_{Na} decay. This finding is consistent with

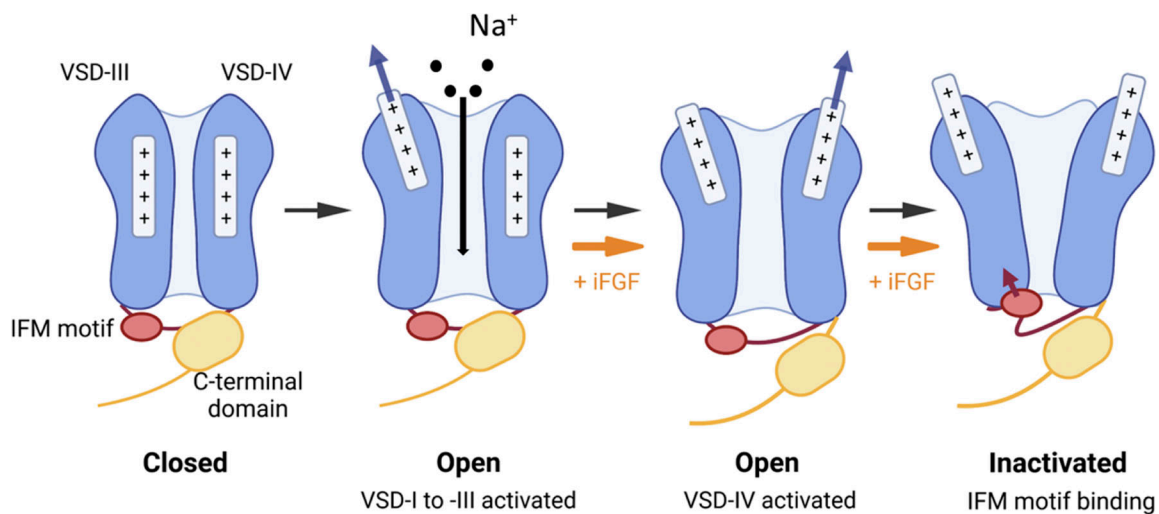


Figure 8. The mechanism of iFGF regulation of the Na_v channel gating. At the resting membrane potential, the closed-state Na_v channel has all voltage sensors (VSD-I–VSD-IV) down in their resting conformations and the activation gate is closed. This schematic portrays two interactions between the resting VSD-IV and the C-terminal domain, and the C-terminal domain and the III–IV linker in the Na_v channel, as proposed by Clairfeuille et al. (2019). The activation of VSD-I to VSD-III leads to the transition of Na_v1.5 from a closed to an open state, allowing for Na⁺ conductance. The resulting activation of VSD-IV facilitates Na_v channel fast inactivation. The coexpression of iFGF facilitates the activation of VSD-IV and thus facilitates the Na_v1.5 channel inactivation.

previous studies demonstrating that the activation of VSD-IV is necessary for initiating fast inactivation (Chahine et al., 1994; Horn et al., 2000; Chanda and Bezanilla, 2002). Additional studies using site-3 toxins, which bind to the extracellular loop near repeat IV S4, showed that intermediate activation of VSD-IV prevents Na_v channel transition into a fast inactivated state (Hanck and Sheets, 2007; Campos et al., 2004). These results imply that the full activation of VSD-IV is required for Na_v fast inactivation (Campos and Beirão, 2006; Campos et al., 2008; Jiang et al., 2021a; Jiang et al., 2021b). According to the cryo-EM structure of mouse Na_v1.5 with α-scorpion toxin, the intermediate-activated VSD-IV made the binding of the IFMT motif less stable and the activation gate wider (Jiang et al., 2021a). The presence of iFGFs facilitates the movement of VSD-IV toward the fully activated state and thus promotes the binding of the IFMT motif or the fast component of inactivation, which also recovers at a faster rate. The competition between two kinetically different pathways of inactivation implies that fast inactivation may limit the contribution of the slow component of inactivation (Richmond et al., 1998; Ransdell et al., 2022). The larger impact on the slope of VSD-IV F–V thus correlates with a larger fraction of the fast component of inactivation (equivalent to reduced %A_{slow}) that can recover faster and partially contribute to increasing channel availability.

iFGF regulation of the Na_v1.5 VSDs

Modulation of VSD-IV is likely the direct effect of iFGF being bound to the Na_v C-terminal domain. A two-switch model for fast inactivation has been proposed based on the chimeric structures of Na_vPaS-hNa_v1.7 in complex with the α-scorpion toxin to link VSD-IV activation and the fast inactivation (Clairfeuille et al., 2019). It is hypothesized that the interaction between resting VSD-IV and Na_v C-terminus, termed switch 1, causes the sequestration of the III–IV linker by the CTD (switch

2), and the activation of VSD-IV alters the CTD conformation to release III–IV linker. We proposed that the binding of iFGF could potentially change the Na_v CTD interaction, mediating earlier activation of VSD-IV (switch 1) and the preceding channel inactivation, as illustrated in the schematic diagram of the iFGF mechanism in Fig. 8.

Additional modulation of the Na_v channel inactivation gate by the iFGF protein(s) is also possible. It has, for example, previously been reported that the E1784K mutation in Na_v1.5 disrupts the switch 2 interaction and results in iFGF12B being ineffective in reducing the persistent component of Na_v1.5-encoded currents (Gade et al., 2020), implying that the interaction between the Na_v III–IV linker and the C-terminal domain is important for the iFGF-mediated modulation of the persistent Na_v current. Another auxiliary protein bound to the Na_v1.5 C-terminal domain, calmodulin, has also been suggested to modulate intramolecular interactions in the Na_v α subunit (Gade et al., 2020), providing an additional mechanism to regulate the persistent Na_v current (Abrams et al., 2020; Chakouri et al., 2022). The binding of iFGF to the Na_v1.5 C-terminal domain, however, might additionally impact the calmodulin-binding conformation (Gabelli et al., 2014) and negatively affect the calmodulin function, as has been demonstrated for Ca²⁺/calmodulin-dependent inactivation of skeletal muscle Na_v1.4-encoded channels (Gardill et al., 2019). Further studies are needed to fully understand the complex interactions, including antagonistic and/or synergistic interactions, and how these impact the regulation/modulation of Na_v channel function by its various auxiliary subunits or combinations of auxiliary subunits.

The modulation of VSD-I activation by iFGF13VY, but not iFGF12B, may be due to the longer N-terminus of iFGF13VY disrupting the coupling between VSDs and resulting in an indirect modulation of VSD-I. Because of the domain-swapped

arrangement in Na_v α subunit, the VSD of one repeat is placed near the S5–S6 linker of the neighboring repeat, allowing two VSDs to be coupled (Chanda et al., 2004). Previous work showed that the binding of local anesthetic drugs inside Na_v channel pores can alter VSD coupling, especially between VSD-I and VSD-IV, resulting in their F–V curves shifting in opposite directions (Muroi and Chanda, 2009). The longer N-terminus of the A-type iFGF isoform, iFGF14A, was also found to localize near the channel intracellular gate where it could regulate the pore (White et al., 2019; Yan et al., 2014). It is therefore possible that the N-terminus of iFGF13VY may remodel VSD coupling, causing altered VSD-I activation as an indirect effect that is connected to VSD-IV modulation.

Conclusion

In this study, we demonstrated distinct effects of iFGF12B and iFGF13VY on the regulation of Na_v1.5 gating kinetics. Our results demonstrate that iFGFs facilitate the outward translation of VSD-IV from resting to activated conformation, leading to a reduction in the slow component of inactivation. The iFGF-specific effects are partially derived from the differential regulation of VSD-IV activation. The ability to modulate the activation of VSD-IV, however, is not unique to the iFGFs. Other regulatory proteins, toxins, and antiarrhythmic drugs can modulate VSD-IV activation and affect Na_v channel inactivation. Taken together, we present a novel mechanism of iFGF modulation of cardiac I_{Na} that accounts for distinct iFGF effects.

Acknowledgments

Olaf S. Andersen served as editor.

The authors thank Dr. A. Burkhalter for assistance with and training in retro-orbital virus injections, Drs. M. Goldfarb and D. Ornitz for providing the *Fgfl2*KO mouse line, Dr. G. Pitt for the polyclonal anti-iFGF13 antibody, and R. Wilson for expert technical assistance.

We gratefully acknowledge the financial support provided by the National Heart Lung and Blood Institute of the NIH (R01 142520 to J.M. Nerbonne and R01 HL150637 to J.M. Nerbonne and J.R. Silva), the NIH National Center for Research Resources (UL1 RR024992 to the Institute for Clinical and Translational Sciences at Washington University), and the Children's Discovery Institute Pediatric Disease Mouse Models Core at Washington University. Viruses were generated in the Hope Center Viral Vectors Core, supported by a Neuroscience Blueprint Core grant (P30 NS057105) at Washington University Medical School. None of these funding sources were involved in study design, data collection, data analyses, data interpretation, manuscript preparation, or the decision to submit this article for consideration for publication.

The authors declare no competing financial interests.

Author contributions: P. Angsutararux, J.M. Nerbonne, and J.R. Silva initiated the project; P. Angsutararux, M. Marras, J.M. Nerbonne, and J.R. Silva supervised the work; P. Angsutararux, A.K. Dutta, M. Marras, C. Abella, R.L. Mellor, and J. Shi conducted the research; P. Angsutararux, J.R. Silva, and J.M. Nerbonne wrote the manuscript. All authors provided edits and feedback.

Submitted: 14 November 2022

Revised: 17 January 2023

Accepted: 9 February 2023

References

- Abrams, J., D. Roybal, N. Chakouri, A.N. Katchman, R. Weinberg, L. Yang, B.X. Chen, S.I. Zakharov, J.A. Hennessey, U.M.R. Avula, et al. 2020. Fibroblast growth factor homologous factors tune arrhythmogenic late NaV1.5 current in calmodulin binding-deficient channels. *JCI Insight*. 5: e141736. <https://doi.org/10.1172/jci.insight.141736>
- Abriel, H. 2010. Cardiac sodium channel Na_v1.5 and interacting proteins: Physiology and pathophysiology. *J. Mol. Cell. Cardiol.* 48:2–11. <https://doi.org/10.1016/j.yjmcc.2009.08.025>
- Abriel, H., and R.S. Kass. 2005. Regulation of the voltage-gated cardiac sodium channel Nav1.5 by interacting proteins. *Trends Cardiovasc. Med.* 15: 35–40. <https://doi.org/10.1016/j.tcm.2005.01.001>
- Ali, S.R., Z. Liu, M.N. Nenov, O. Folorunso, A. Singh, F. Scala, H. Chen, T.F. James, M. Alshammari, N.I. Panova-Elektronova, et al. 2018. Functional modulation of voltage-gated sodium channels by a FGF14-based peptidomimetic. *ACS Chem. Neurosci.* 9:976–987. <https://doi.org/10.1021/acscchemneuro.7b00399>
- Angsutararux, P., P.W. Kang, W. Zhu, and J.R. Silva. 2021a. Conformations of voltage-sensing domain III differentially define NaV channel closed- and open-state inactivation. *J. Gen. Physiol.* 153:e202112891. <https://doi.org/10.1085/jgp.202112891>
- Angsutararux, P., W. Zhu, T.L. Voelker, and J.R. Silva. 2021b. Molecular pathology of sodium channel beta-subunit variants. *Front. Pharmacol.* 12: 761275. <https://doi.org/10.3389/fphar.2021.761275>
- Barbosa, C., Y. Xiao, A.J. Johnson, W. Xie, J.A. Strong, J.M. Zhang, and T.R. Cummins. 2017. FHF2 isoforms differentially regulate Nav1.6-mediated resurgent sodium currents in dorsal root ganglion neurons. *Pflugers Arch.* 469:195–212. <https://doi.org/10.1007/s00424-016-1911-9>
- Brunet, S., F. Aimond, H. Li, W. Guo, J. Eldstrom, D. Fedida, K.A. Yamada, and J.M. Nerbonne. 2004. Heterogeneous expression of repolarizing, voltage-gated K⁺ currents in adult mouse ventricles. *J. Physiol.* 559: 103–120. <https://doi.org/10.1113/jphysiol.2004.063347>
- Burel, S., F.C. Coyan, M. Lorenzini, M.R. Meyer, C.F. Lichti, J.H. Brown, G. Loussouarn, F. Charpentier, J.M. Nerbonne, R.R. Townsend, et al. 2017. C-terminal phosphorylation of Na_v1.5 impairs FGF13-dependent regulation of channel inactivation. *J. Biol. Chem.* 292:17431–17448. <https://doi.org/10.1074/jbc.M117.787788>
- Calhoun, J.D., and L.L. Isom. 2014. The role of non-pore-forming β subunits in physiology and pathophysiology of voltage-gated sodium channels. *Handb. Exp. Pharmacol.* 221:51–89. https://doi.org/10.1007/978-3-642-41588-3_4
- Campos, F.V., and P.S.L. Beirão. 2006. Effects of bound ts3 on voltage dependence of sodium channel transitions to and from inactivation and energetics of its unbinding. *Cell Biochem. Biophys.* 44:424–430. <https://doi.org/10.1385/CBB:44:3:424>
- Campos, F.V., F.I.V. Coronas, and P.S.L. Beirão. 2004. Voltage-dependent displacement of the scorpion toxin Ts3 from sodium channels and its implication on the control of inactivation. *Br. J. Pharmacol.* 142:1115–1122. <https://doi.org/10.1038/sj.bjph.0705793>
- Campos, F.V., B. Chanda, P.S.L. Beirão, and F. Bezanilla. 2008. α-scorpion toxin impairs a conformational change that leads to fast inactivation of muscle sodium channels. *J. Gen. Physiol.* 132:251–263. <https://doi.org/10.1085/jgp.20080995>
- Capes, D.L., M.P. Goldschen-Ohm, M. Arcisio-Miranda, F. Bezanilla, and B. Chanda. 2013. Domain IV voltage-sensor movement is both sufficient and rate limiting for fast inactivation in sodium channels. *J. Gen. Physiol.* 142:101–112. <https://doi.org/10.1085/jgp.201310998>
- Chahine, M., A.L. George Jr, M. Zhou, S. Ji, W. Sun, R.L. Barchi, and R. Horn. 1994. Sodium channel mutations in paramyotonia congenita uncouple inactivation from activation. *Neuron.* 12:281–294. [https://doi.org/10.1016/0896-6273\(94\)90271-2](https://doi.org/10.1016/0896-6273(94)90271-2)
- Chakouri, N., S. Rivas, D. Roybal, L. Yang, J. Diaz, A. Hsu, R. Mahling, B.X. Chen, J.O. Owoyemi, D. DiSilvestre, et al. 2022. Fibroblast growth factor homologous factors serve as a molecular rheostat in tuning arrhythmogenic cardiac late sodium current. *Nat. Cardiovasc. Res.* 1:1–13. <https://doi.org/10.1038/s44161-022-00060-6>
- Chanda, B., and F. Bezanilla. 2002. Tracking voltage-dependent conformational changes in skeletal muscle sodium channel during activation. *J. Gen. Physiol.* 120:629–645. <https://doi.org/10.1085/jgp.20028679>

- Chanda, B., O.K. Asamoah, and F. Bezanilla. 2004. Coupling interactions between voltage sensors of the sodium channel as revealed by site-specific measurements. *J. Gen. Physiol.* 123:217–230. <https://doi.org/10.1085/jgp.200308971>
- Clairfeuille, T., A. Cloake, D.T. Infield, J.P. Llongueras, C.P. Arthur, Z.R. Li, Y. Jian, M.F. Martin-Eauclaire, P.E. Bougis, C. Ciferri, et al. 2019. Structural basis of α -scorpion toxin action on Na_v channels. *Science*. 363: eaav8573. <https://doi.org/10.1126/science.aav8573>
- de Kok, J.B., R.W. Roelofs, B.A. Giesendorf, J.L. Pennings, E.T. Waas, T. Feuth, D.W. Swinkels, and P.N. Span. 2005. Normalization of gene expression measurements in tumor tissues: Comparison of 13 endogenous control genes. *Lab. Invest.* 85:154–159. <https://doi.org/10.1038/labinvest.3700208>
- Dhar Malhotra, J., C. Chen, I. Rivolta, H. Abriel, R. Malhotra, L.N. Mattei, F.C. Brosius, R.S. Kass, and L.L. Isom. 2001. Characterization of sodium channel α - and β -subunits in rat and mouse cardiac myocytes. *Circulation*. 103:1303–1310. <https://doi.org/10.1161/01.CIR.103.9.1303>
- Doudna, J.A., and E. Charpentier. 2014. Genome editing. The new frontier of genome engineering with CRISPR-Cas9. *Science*. 346:1258096. <https://doi.org/10.1126/science.1258096>
- Gabelli, S.B., A. Boto, V.H. Kuhns, M.A. Bianchet, F. Farinelli, S. Aripirala, J. Yoder, J. Jakoncic, G.F. Tomaselli, and L.M. Amzel. 2014. Regulation of the Nav1.5 cytoplasmic domain by calmodulin. *Nat. Commun.* 5:5126. <https://doi.org/10.1038/ncomms6126>
- Gade, A.R., S.O. Marx, and G.S. Pitt. 2020. An interaction between the III-IV linker and CTD in Nav1.5 confers regulation of inactivation by CaM and FHF. *J. Gen. Physiol.* 152:e201912434. <https://doi.org/10.1085/jgp.201912434>
- Gandhi, C.S., and R. Olcese. 2008. The voltage-clamp fluorometry technique. *Methods Mol. Biol.* 491:213–231. https://doi.org/10.1007/978-1-59745-526-8_17
- Gardill, B.R., R.E. Rivera-Acevedo, C.C. Tung, and F. Van Petegem. 2019. Crystal structures of Ca²⁺-calmodulin bound to Nav_v C-terminal regions suggest role for EF-hand domain in binding and inactivation. *Proc. Natl. Acad. Sci. USA*. 116:10763–10772. <https://doi.org/10.1073/pnas.1818618116>
- Goetz-R., K.Dover, F.Laezza, N.Shtreizent, X.Huang, D.Tchetchik, A.V.Eli-seenkova, C.F.Xu, T.A.Neubert, D.M.Ornitz, et al. 2009. Crystal structure of a fibroblast growth factor homologous factor (FHF) defines a conserved surface on FHFs for binding and modulation of voltage-gated sodium channels. *J. Biol. Chem.* 284:17883–17896. <https://doi.org/10.1074/jbc.M109.001842>
- Goldfarb, M. 2005. Fibroblast growth factor homologous factors: Evolution, structure, and function. *Cytokine Growth Factor Rev.* 16:215–220. <https://doi.org/10.1016/j.cytogfr.2005.02.002>
- Goldfarb, M., J. Schoorlemmer, A. Williams, S. Diwakar, Q. Wang, X. Huang, J. Giza, D. Tchetchik, K. Kelley, A. Vega, et al. 2007. Fibroblast growth factor homologous factors control neuronal excitability through modulation of voltage-gated sodium channels. *Neuron*. 55:449–463. <https://doi.org/10.1016/j.neuron.2007.07.006>
- Hanck, D.A., and M.F. Sheets. 2007. Site-3 toxins and cardiac sodium channels. *Toxicol.* 49:181–193. <https://doi.org/10.1016/j.toxicol.2006.09.017>
- Hennessey, J.A., C.A. Marcou, C. Wang, E.Q. Wei, C. Wang, D.J. Tester, M. Torchio, F. Dagradi, L. Crotti, P.J. Schwartz, et al. 2013. FGF12 is a candidate Brugada syndrome locus. *Heart Rhythm*. 10:1886–1894. <https://doi.org/10.1016/j.hrthm.2013.09.064>
- Horn, R., S. Ding, and H.J. Gruber. 2000. Immobilizing the moving parts of voltage-gated ion channels. *J. Gen. Physiol.* 116:461–476. <https://doi.org/10.1085/jgp.116.3.461>
- Hsu, E.J., W. Zhu, A.R. Schubert, T. Voelker, Z. Varga, and J.R. Silva. 2017. Regulation of Na⁺ channel inactivation by the DIII and DIV voltage-sensing domains. *J. Gen. Physiol.* 149:389–403. <https://doi.org/10.1085/jgp.201611678>
- Iqbal, S.M., and R. Lemmens-Gruber. 2019. Phosphorylation of cardiac voltage-gated sodium channel: Potential players with multiple dimensions. *Acta Physiol.* 225:e13210. <https://doi.org/10.1111/apha.13210>
- Jiang, D., L.Tonggu, T.M.Gamal El-Din, R.Banh, R.Pomès, N.Zheng, W.A.Catterall. 2021a. Structural basis for voltage-sensor trapping of the cardiac sodium channel by a deathstalker scorpion toxin. *Nat. Commun.* 12:128. <https://doi.org/10.1038/s41467-020-20078-3>
- Jiang, D., R.Banh, T.M.Gamal El-Din, L.Tonggu, M.J.Lenaeus, R.Pomès, N.Zheng, and W.A.Catterall. 2021b. Open-state structure and pore gating mechanism of the cardiac sodium channel. *Cell*. 184: 5151–5162.e11. <https://doi.org/10.1016/j.cell.2021.08.021>
- Laezza, F., A. Lampert, M.A. Kozel, B.R. Gerber, A.M. Rush, J.M. Nerbonne, S.G. Waxman, S.D. Dib-Hajj, and D.M. Ornitz. 2009. FGF14 N-terminal splice variants differentially modulate Nav1.2 and Nav1.6-encoded sodium channels. *Mol. Cell. Neurosci.* 42:90–101. <https://doi.org/10.1016/j.mcn.2009.05.007>
- Li, Q., Y. Zhao, G. Wu, S. Chen, Y. Zhou, S. Li, M. Zhou, Q. Fan, J. Pu, K. Hong, et al. 2017. De novo FGF12 (fibroblast growth factor 12) functional variation is potentially associated with idiopathic ventricular tachycardia. *J. Am. Heart Assoc.* 6:e006130. <https://doi.org/10.1161/JAHA.117.006130>
- Liu, C.J., S.D. Dib-Hajj, and S.G. Waxman. 2001. Fibroblast growth factor homologous factor 1B binds to the C terminus of the tetrodotoxin-resistant sodium channel rNav1.9a (NaN). *J. Biol. Chem.* 276:18925–18933. <https://doi.org/10.1074/jbc.M101606200>
- Liu, C.J., S.D. Dib-Hajj, M. Renganathan, T.R. Cummins, and S.G. Waxman. 2003. Modulation of the cardiac sodium channel Nav1.5 by fibroblast growth factor homologous factor 1B. *J. Biol. Chem.* 278:1029–1036. <https://doi.org/10.1074/jbc.M207074200>
- Lopez-Santiago, L.F., L.S. Meadows, S.J. Ernst, C. Chen, D. Malhotra, D.P. McEwen, A. Speelman, J.L. Noebels, S.K. Maier, A.N. Lopatin, et al. 2007. Sodium channel Scn1b null mice exhibit prolonged QT and RR intervals. *J. Mol. Cell Cardiol.* 43:636–647. <https://doi.org/10.1016/j.yjmcc.2007.07.062>
- Lorenzini, M., S. Burel, A. Lesage, E. Wagner, C. Charrière, P.M. Chevillard, B. Evrard, D. Maloney, K.M. Ruff, R.V. Pappu, et al. 2021. Proteomic and functional mapping of cardiac Nav1.5 channel phosphorylation sites. *J. Gen. Physiol.* 153:e202012646. <https://doi.org/10.1085/jgp.202012646>
- Lou, J.Y., F. Laezza, B.R. Gerber, M. Xiao, K.A. Yamada, H. Hartmann, A.M. Craig, J.M. Nerbonne, and D.M. Ornitz. 2005. Fibroblast growth factor 14 is an intracellular modulator of voltage-gated sodium channels. *J. Physiol.* 569:179–193. <https://doi.org/10.1113/jphysiol.2005.097220>
- Maier, S.K.G., R.E. Westenbroek, K.A. McCormick, R. Curtis, T. Scheuer, and W.A. Catterall. 2004. Distinct subcellular localization of different sodium channel α and β subunits in single ventricular myocytes from mouse heart. *Circulation*. 109:1421–1427. <https://doi.org/10.1161/01.CIR.0000121421.61896.24>
- Mangold, K.E., B.D. Brumback, P. Angsutararux, T.L. Voelker, W. Zhu, P.W. Kang, J.D. Moreno, and J.R. Silva. 2017. Mechanisms and models of cardiac sodium channel inactivation. *Channels*. 11:517–533. <https://doi.org/10.1080/19336950.2017.1369637>
- Mannuzzu, L.M., M.M. Moronne, and E.Y. Isacoff. 1996. Direct physical measure of conformational rearrangement underlying potassium channel gating. *Science*. 271:213–216. <https://doi.org/10.1126/science.271.5246.213>
- Marionneau, C., S. Brunet, T.P. Flagg, T.K. Pilgram, S. Demolombe, and J.M. Nerbonne. 2008. Distinct cellular and molecular mechanisms underlie functional remodeling of repolarizing K⁺ currents with left ventricular hypertrophy. *Circ. Res.* 102:1406–1415. <https://doi.org/10.1161/CIRCRESAHA.107.170050>
- Meadows, L.S., and L.L. Isom. 2005. Sodium channels as macromolecular complexes: Implications for inherited arrhythmia syndromes. *Cardiovasc. Res.* 67:448–458. <https://doi.org/10.1016/j.cardiores.2005.04.003>
- Munoz-Sanjuan, I., P.M. Smallwood, and J. Nathans. 2000. Isoform diversity among fibroblast growth factor homologous factors is generated by alternative promoter usage and differential splicing. *J. Biol. Chem.* 275: 2589–2597. <https://doi.org/10.1074/jbc.275.4.2589>
- Muroi, Y., and B. Chanda. 2009. Local anesthetics disrupt energetic coupling between the voltage-sensing segments of a sodium channel. *J. Gen. Physiol.* 133:1–15. <https://doi.org/10.1085/jgp.200810103>
- Musa, H., C.F. Kline, A.C. Sturm, N. Murphy, S. Adelman, C. Wang, H. Yan, B.L. Johnson, T.A. Csepe, A. Kilic, et al. 2015. SCN5A variant that blocks fibroblast growth factor homologous factor regulation causes human arrhythmia. *Proc. Natl. Acad. Sci. USA*. 112:12528–12533. <https://doi.org/10.1073/pnas.1516430112>
- Nerbonne, J.M., and R.S. Kass. 2005. Molecular physiology of cardiac repolarization. *Physiol. Rev.* 85:1205–1253. <https://doi.org/10.1152/physrev.00002.2005>
- Noble, D., and P.J. Noble. 2006. Late sodium current in the pathophysiology of cardiovascular disease: Consequences of sodium-calcium overload. *Heart*. 92:iv1–iv5. <https://doi.org/10.1136/hrt.2005.078782>
- Olsen, S.K., M. Garbi, N. Zampieri, A.V. Eliseenkova, D.M. Ornitz, M. Goldfarb, and M. Mohammadi. 2003. Fibroblast growth factor (FGF) homologous factors share structural but not functional homology with FGFs. *J. Biol. Chem.* 278:34226–34236. <https://doi.org/10.1074/jbc.M303183200>
- Pablo, J.L., and G.S. Pitt. 2017. Fibroblast growth factor homologous factors (FHFs): New roles in neuronal health and disease. *Neuroscientist*. 22: 19–25. <https://doi.org/10.1177/1073858414562217>

- Park, D.S., A. Shekhar, C. Marra, X. Lin, C. Vasquez, S. Solinas, K. Kelley, G. Morley, M. Goldfarb, and G.I. Fishman. 2016. Fhf2 gene deletion causes temperature-sensitive cardiac conduction failure. *Nat. Commun.* 7: 12966. <https://doi.org/10.1038/ncomms12966>
- Park, D.S., A. Shekhar, J. Santucci III, G. Redel-Traub, S. Solinas, S. Mintz, X. Lin, E.W. Chang, D. Narke, Y. Xia, et al. 2020. Ionic mechanisms of impulse propagation failure in the FHF2-deficient heart. *Circ. Res.* 127: 1536–1548. <https://doi.org/10.1161/CIRCRESAHA.120.317349>
- Pitt, G.S., and S.Y. Lee. 2016. Current view on regulation of voltage-gated sodium channels by calcium and auxiliary proteins. *Protein Sci.* 25: 1573–1584. <https://doi.org/10.1002/pro.2960>
- Pugach, E.K., P.A. Richmond, J.G. Azofeifa, R.D. Dowell, and L.A. Leinwand. 2015. Prolonged Cre expression driven by the α -myosin heavy chain promoter can be cardiotoxic. *J. Mol. Cell. Cardiol.* 86:54–61. <https://doi.org/10.1016/j.yjmcc.2015.06.019>
- Ransdell, J.L., J.D. Moreno, D. Bhagavan, J.R. Silva, and J.M. Nerbonne. 2022. Intrinsic mechanisms in the gating of resurgent Na⁺ currents. *eLife.* 11: 20220125. <https://doi.org/10.7554/eLife.70173>
- Richmond, J.E., D.E. Featherstone, H.A. Hartmann, and P.C. Ruben. 1998. Slow inactivation in human cardiac sodium channels. *Biophys. J.* 74: 2945–2952. [https://doi.org/10.1016/S0006-3495\(98\)78001-4](https://doi.org/10.1016/S0006-3495(98)78001-4)
- Ruan, Y., N. Liu, and S.G. Priori. 2009. Sodium channel mutations and arrhythmias. *Nat. Rev. Cardiol.* 6:337–348. <https://doi.org/10.1038/nrcardio.2009.44>
- Rudokas, M.W., Z. Varga, A.R. Schubert, A.B. Asaro, and J.R. Silva. 2014. The *Xenopus* oocyte cut-open vaseline gap voltage-clamp technique with fluorometry. *J. Vis. Exp.* 11:51040. <https://doi.org/10.3791/51040>
- Schmittgen, T.D., and K.J. Livak. 2008. Analyzing real-time PCR data by the comparative C_T method. *Nat. Protoc.* 3:1101–1108. <https://doi.org/10.1038/nprot.2008.73>
- Sentmanat, M.F., J.M. White, E. Kouranova, and X. Cui. 2022. Highly reliable creation of floxed alleles by electroporating single-cell embryos. *BMC Biol.* 20:31. <https://doi.org/10.1186/s12915-021-01223-w>
- Silva, J. 2014. Slow inactivation of Na⁺ channels. *Handb. Exp. Pharmacol.* 221: 33–49. https://doi.org/10.1007/978-3-642-41588-3_3
- Silva, J.R. and S.A. Goldstein. 2013a. Voltage-sensor movements describe slow inactivation of voltage-gated sodium channels I: Wild-type skeletal muscle Na_v1.4. *J. Gen. Physiol.* 141:309–321. <https://doi.org/10.1085/jgp.201210909>
- Silva, J.R. and S.A. Goldstein. 2013b. Voltage-sensor movements describe slow inactivation of voltage-gated sodium channels II: A periodic paralysis mutation in Na_v1.4 (L689I). *J. Gen. Physiol.* 141:323–334. <https://doi.org/10.1085/jgp.201210910>
- Singh, A.K., P.A. Wadsworth, C.M. Tapia, G. Aceto, S.R. Ali, H. Chen, M. D'Ascenzo, J. Zhou, and F. Laezza. 2020. Mapping of the FGF14:Nav1.6 complex interface reveals FLPK as a functionally active peptide modulating excitability. *Physiol. Rep.* 8:e14505. <https://doi.org/10.14814/phy2.14505>
- Singh, A.K., N.M. Dvorak, C.M. Tapia, A. Mosebarger, S.R. Ali, Z. Bullock, H. Chen, J. Zhou, and F. Laezza. 2021. Differential modulation of the voltage-gated Na⁺ channel 1.6 by peptides derived from fibroblast growth factor 14. *Front. Mol. Biosci.* 8:742903. <https://doi.org/10.3389/fmolb.2021.742903>
- Stefani, E. and F. Bezanilla. 1998. Cut-open oocyte voltage-clamp technique. *Methods Enzymol.* 293:300–318. [https://doi.org/10.1016/S0076-6879\(98\)93020-8](https://doi.org/10.1016/S0076-6879(98)93020-8)
- Ton, A.T., W. Nguyen, K. Sweat, Y. Miron, E. Hernandez, T. Wong, V. Geft, A. Macias, A. Espinoza, K. Truong, et al. 2021. Arrhythmogenic and anti-arrhythmic actions of late sustained sodium current in the adult human heart. *Sci. Rep.* 11:12014. <https://doi.org/10.1038/s41598-021-91528-1>
- Varga, Z., W. Zhu, A.R. Schubert, J.L. Pardieck, A. Krumholz, E.J. Hsu, M.A. Zaydman, J. Cui, and J.R. Silva. 2015. Direct measurement of cardiac Na⁺ channel conformations reveals molecular pathologies of inherited mutations. *Circ. Arrhythm. Electrophysiol.* 8:1228–1239. <https://doi.org/10.1161/CIRCEP.115.003155>
- Velišková, J., C. Marra, Y. Liu, A. Shekhar, D.S. Park, V. Iatckova, Y. Xie, G.I. Fishman, L. Velišek, and M. Goldfarb. 2021. Early onset epilepsy and sudden unexpected death in epilepsy with cardiac arrhythmia in mice carrying the early infantile epileptic encephalopathy 47 gain-of-function FHF1(FGF12) missense mutation. *Epilepsia.* 62:1546–1558. <https://doi.org/10.1111/epi.16916>
- Wang, C., J.A. Hennessey, R.D. Kirkton, C. Wang, V. Graham, R.S. Puranam, P.B. Rosenberg, N. Bursac, and G.S. Pitt. 2011a. Fibroblast growth factor homologous factor 13 regulates Na⁺ channels and conduction velocity in murine hearts. *Circ. Res.* 109:775–782. <https://doi.org/10.1161/CIRCRESAHA.111.247957>
- Wang, C., C. Wang, E.G. Hoch, and G.S. Pitt. 2011b. Identification of novel interaction sites that determine specificity between fibroblast growth factor homologous factors and voltage-gated sodium channels. *J. Biol. Chem.* 286:24253–24263. <https://doi.org/10.1074/jbc.M111.245803>
- Wang, C., B.C. Chung, H. Yan, S.Y. Lee, and G.S. Pitt. 2012. Crystal structure of the ternary complex of a Nav C-terminal domain, a fibroblast growth factor homologous factor, and calmodulin. *Structure.* 20:1167–1176. <https://doi.org/10.1016/j.str.2012.05.001>
- Wang, C., B.C. Chung, H. Yan, H.G. Wang, S.Y. Lee, and G.S. Pitt. 2014. Structural analyses of Ca²⁺/CaM interaction with Nav channel C-termini reveal mechanisms of calcium-dependent regulation. *Nat. Commun.* 5: 4896. <https://doi.org/10.1038/ncomms5896>
- Wang, X., H. Tang, E.Q. Wei, Z. Wang, J. Yang, R. Yang, S. Wang, Y. Zhang, G.S. Pitt, H. Zhang, and C. Wang. 2017. Conditional knockout of Fgf13 in murine hearts increases arrhythmia susceptibility and reveals novel ion channel modulatory roles. *J. Mol. Cell. Cardiol.* 104:63–74. <https://doi.org/10.1016/j.yjmcc.2017.01.009>
- White, H.V., S.T. Brown, T.C. Bozza, and I.M. Raman. 2019. Effects of FGF14 and Nav β 4 deletion on transient and resurgent Na current in cerebellar Purkinje neurons. *J. Gen. Physiol.* 151:1300–1318. <https://doi.org/10.1085/jgp.201912390>
- Xu, H., W. Guo, and J.M. Nerbonne. 1999. Four kinetically distinct depolarization-activated K⁺ currents in adult mouse ventricular myocytes. *J. Gen. Physiol.* 113:661–678. <https://doi.org/10.1085/jgp.113.5.661>
- Yan, H., J.L. Pablo, C. Wang, and G.S. Pitt. 2014. FGF14 modulates resurgent sodium current in mouse cerebellar Purkinje neurons. *Elife.* 3:e04193. <https://doi.org/10.7554/eLife.04193>
- Yang, J., Z. Wang, D.S. Sinden, X. Wang, B. Shan, X. Yu, H. Zhang, G.S. Pitt, and C. Wang. 2016. FGF13 modulates the gating properties of the cardiac sodium channel Na_v1.5 in an isoform-specific manner. *Channels.* 10: 410–420. <https://doi.org/10.1080/19336950.2016.1190055>
- Yu, F.H., and W.A. Catterall. 2003. Overview of the voltage-gated sodium channel family. *Genome Biol.* 4:207. <https://doi.org/10.1186/gb-2003-4-3-207>
- Zhu, W., Z. Varga, and J.R. Silva. 2016. Molecular motions that shape the cardiac action potential: Insights from voltage clamp fluorometry. *Prog. Biophys. Mol. Biol.* 120:3–17. <https://doi.org/10.1016/j.pbiomolbio.2015.12.003>
- Zhu, W., T.L. Voelker, Z. Varga, A.R. Schubert, J.M. Nerbonne, and J.R. Silva. 2017. Mechanisms of noncovalent β subunit regulation of Na_v channel gating. *J. Gen. Physiol.* 149:813–831. <https://doi.org/10.1085/jgp.201711802>
- Zhu, W., W. Wang, P. Angsutararux, R.L. Mellor, L.L. Isom, J.M. Nerbonne, and J.R. Silva. 2021. Modulation of the effects of class Ib antiarrhythmics on cardiac Na_v1.5-encoded channels by accessory Na_v β subunits. *JCI Insight.* 6:143092. <https://doi.org/10.1172/jci.insight.143092>
- Zolotukhin, S., M. Potter, I. Zolotukhin, Y. Sakai, S. Loiler, T.J. Fraitas, Jr., V.A. Chiodo, T. Phillipsberg, N. Muzyczka, W.W. Hauswirth, et al. 2002. Production and purification of serotype 1, 2, and 5 recombinant adeno-associated viral vectors. *Methods.* 28:158–167. [https://doi.org/10.1016/s1046-2023\(02\)00220-7](https://doi.org/10.1016/s1046-2023(02)00220-7)

Supplemental material

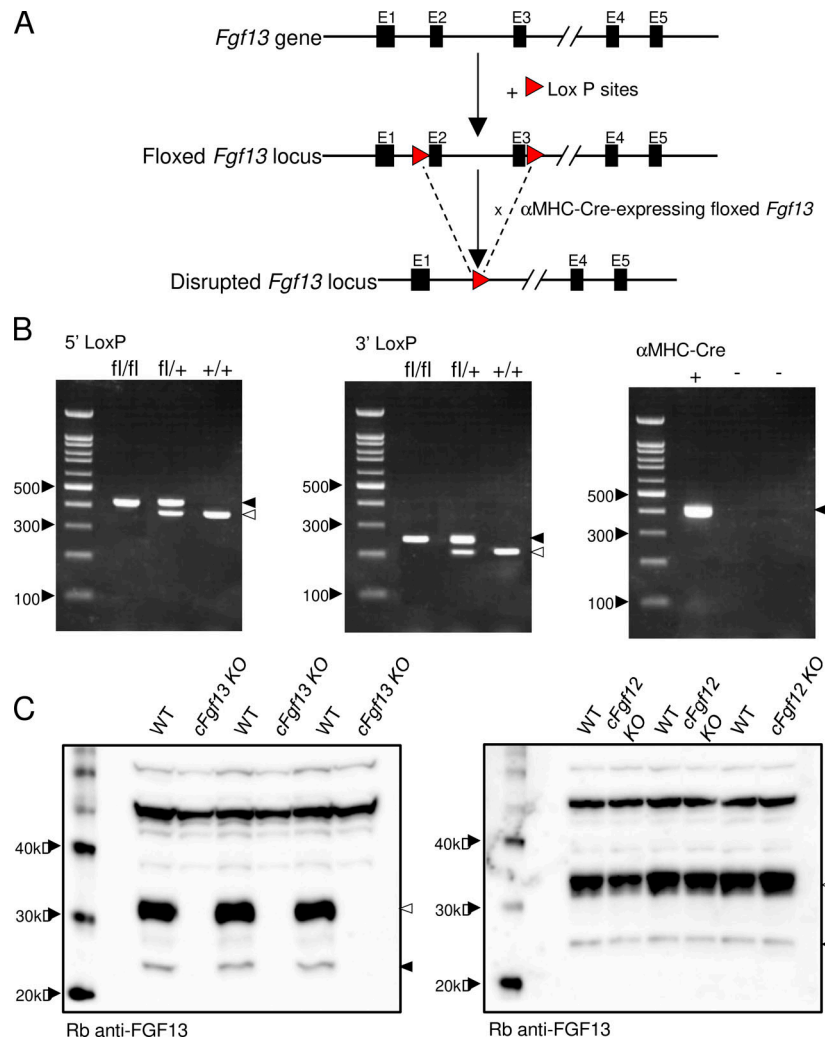


Figure S1. Targeted disruption of the *Fgf13* locus and generation/validation of cardiac-specific *Fgf13* targeted deletion mice. (A) Schematics of the endogenous *Fgf13* locus (top), located on the X chromosome, and the floxed *Fgf13* locus (middle). Following sequencing of the first and second generation of offspring, heterozygous *Fgf13* floxed (*Fgf13^{fl/+}*) female mice and hemizygous *Fgf13* floxed (*Fgf13^{fl/y}*) male mice were crossed to also generate homozygous *Fgf13* floxed (*Fgf13^{fl/fl}*) females. The *Fgf13^{fl/y}* and *Fgf13^{fl/fl}* animals were then crossed with transgenic mice expressing Cre recombinase driven by the cardiac-specific α -MHC promoter. Crossing the Cre recombinase positive, hemizygous floxed male (*Fgf13^{fl/y}*) offspring with *Fgf13^{fl/fl}* females (or Cre recombinase heterozygous *Fgf13^{fl/+}* females with *Fgf13^{fl/y}* males) provided cardiac-specific *Fgf13* targeted deletion hemizygous male and homozygous female animals, referred to collectively here as cardiac-specific *Fgf13* knockouts, *cFgf13KO*. Three sets of primers were employed to detect the 5' LoxP site, the 3' LoxP site, and the α -MHC-driven Cre-recombinase (see Materials and methods). **(B)** Representative results from PCR analyses of homozygous *Fgf13^{fl/fl}*, heterozygous *Fgf13^{fl/+}*, and WT (*+/+*) female mice using primers targeting the 5' LoxP site (left) and the 3' LoxP site (middle) are shown. Further screening of these animals with primers to the α -MHC-Cre-recombinase transgene identified Cre recombinase positive animals (right). **(C)** Western blot analyses confirmed loss of iFGF13 protein expression. Protein lysates (1 μ g), prepared from WT, *cFgf13KO*, and *Fgf12* targeted deletion (*Fgf12KO*) ventricles, were fractionated, transferred, and membranes were probed with an anti-iFGF13 antibody, as described in Materials and methods. A prominent band at \sim 32 kD and a faint band at \sim 24 kD were detected with the anti-iFGF13 antibody in the WT (left and right panels) and *Fgf12KO* (right panel) LV protein samples, whereas these bands were not detected in the *cFgf13KO* LV samples (left panel), consistent with the elimination of iFGF13 proteins. Source data are available for this figure: SourceData FS1.

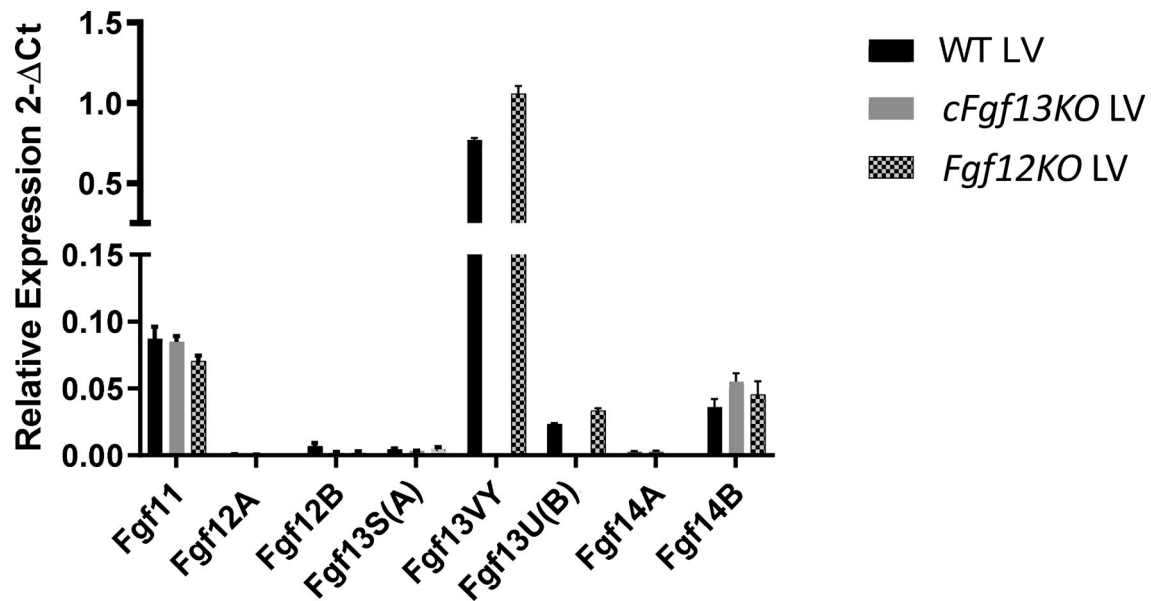


Figure S2. Loss of *Fgf13* or *Fgf12* does not measurably affect the expression levels of other *Fgf* transcripts in adult mouse LV. The expression levels of the *Fgf11*, *Fgf12A*, *Fgf12B*, *Fgf13S(A)*, *Fgf13VY*, *Fgf13U(B)*, *Fgf14A*, and *Fgf14B* transcripts in WT, *cFgf13KO*, and *Fgf12KO* LV samples were measured and normalized to *Hprt* expression in the same sample, as described in Materials and methods. These analyses revealed that the *Fgf13* transcripts are undetectable in *cFgf13KO* LV. In addition, the mean \pm SEM relative expression levels of the other *Fgf* transcripts in *cFgf13KO* and WT LV are indistinguishable.

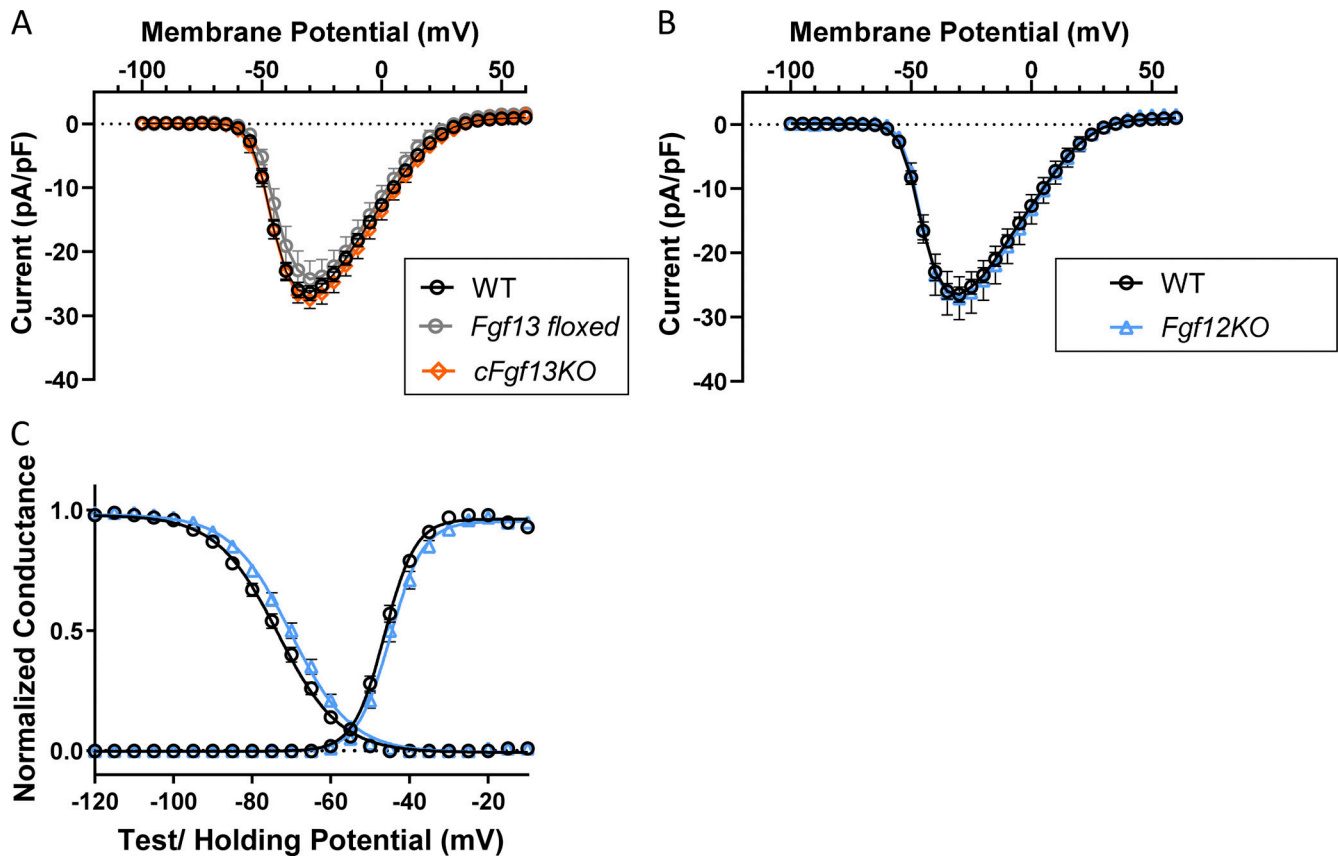


Figure S3. The amplitudes/densities of I_{Na} in mouse LV myocytes are not affected by the loss of iFGF13, and the properties of I_{Na} in mouse LV myocytes are not affected by the loss of iFGF12. (A) The cardiac-specific deletion of *Fgf13* does not affect peak I_{Na} densities in LV myocytes: peak I_{Na} densities at all voltages in WT, *Fgf13 floxed*, and *cFgf13KO* mouse LV myocytes are not significantly different (P values >0.15 at all voltages). (B and C) Consistent with the negligible expression of *Fgf12* transcripts in adult mouse LV (see Fig. S2), peak I_{Na} densities at all voltages (B) and the voltage-dependencies of I_{Na} activation and inactivation (C) determined in adult *Fgf12KO* LV myocytes are indistinguishable (P values >0.13) from I_{Na} in WT LV myocytes at all voltages.

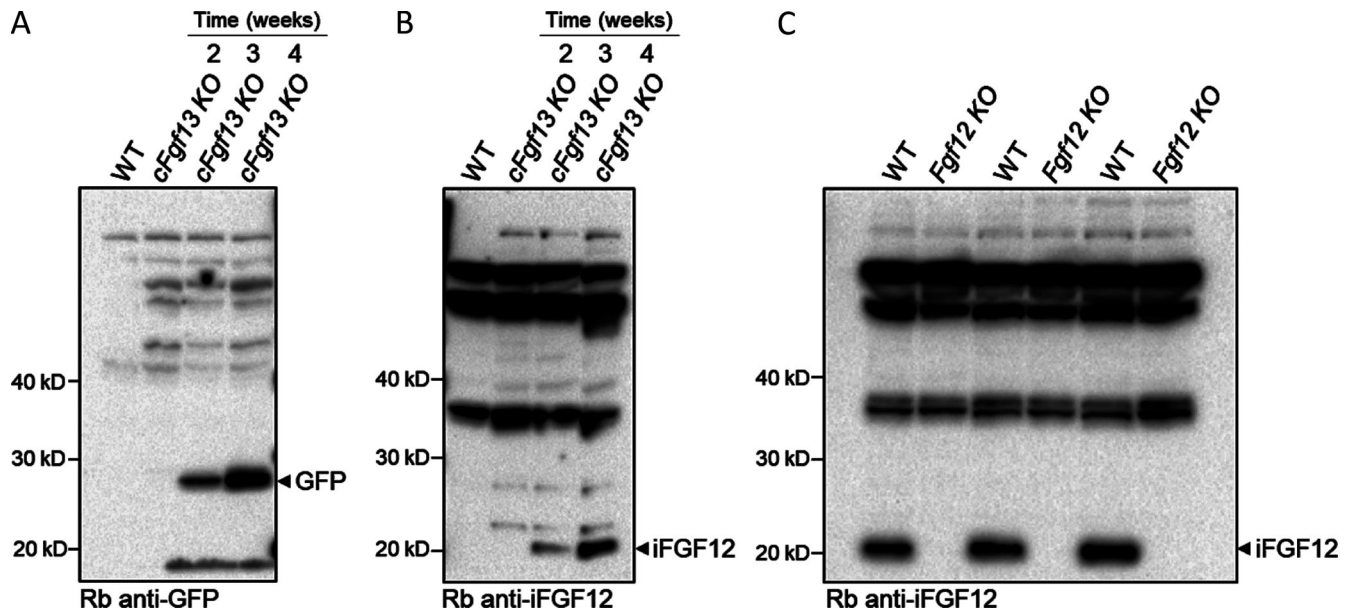


Figure S4. **The time-dependence of AAV9-mediated expression of iFGF12B and eGFP in adult mouse LV and the validation of the anti-iFGF12 antibody.** (A and B) Western blots of fractionated protein lysates prepared from *cFgf13KO* ventricles 2, 3, or 4 wk following retro-orbital injections of a 1:1 mixture of the hFGF12B-expressing and eGFP-expressing AAV9 viruses, probed with an anti-EGFP (A) or anti-iFGF12 (B) antibody, as described in Materials and methods. (C) To validate the anti-iFGF12 antibody used in the Western blot in B, protein lysates prepared from WT and *Fgf12KO* adult mouse left and right atria were fractionated, transferred, and the membranes were probed with an anti-iFGF12 antibody, as described in Materials and methods. A prominent band at ~20 kD was detected with the anti-iFGF12 antibody in the WT, but not in the *Fgf12KO*, atrial protein samples, consistent with the elimination of iFGF12 proteins and validating the anti-iFGF12 antibody for Western blot analyses of iFGF12 protein expression. Source data are available for this figure: SourceData FS4.

Downloaded from http://jgp.physiology.org/jgp/article-pdf/155/5/e202213300/1449616/jgp_202213300.pdf by Washington University in St. Louis Libraries user on 23 April 2023

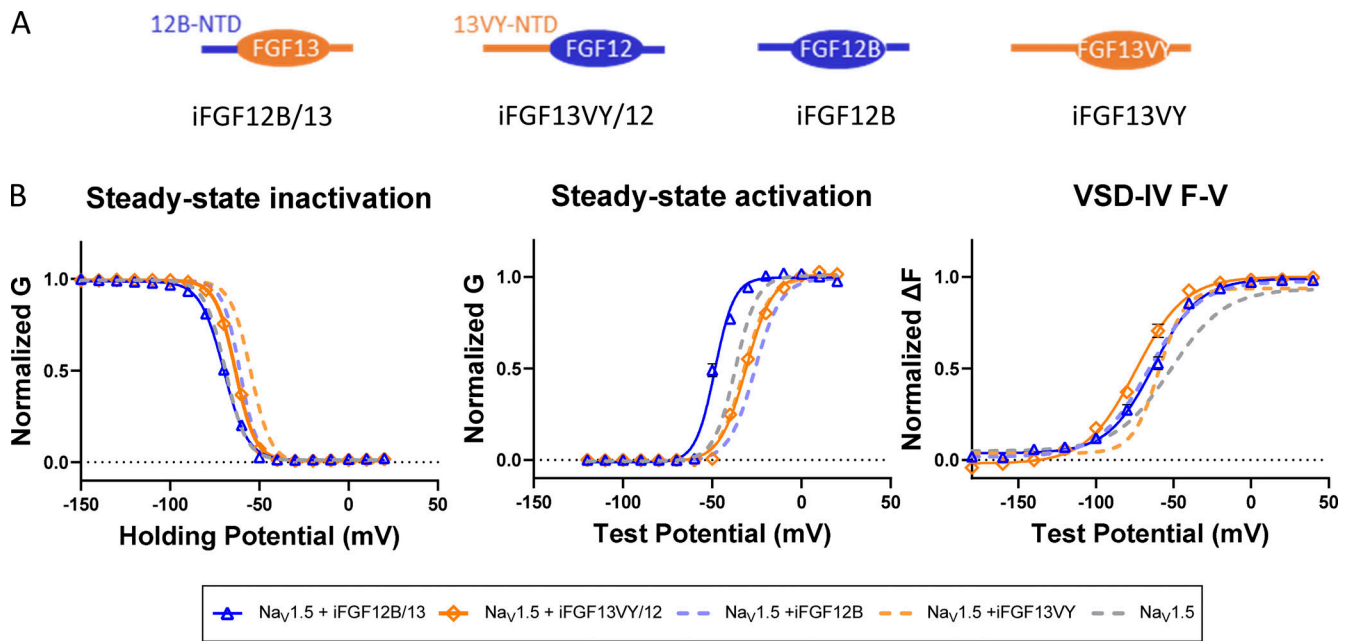


Figure S5. **Switching N-terminal domains between iFGF12B and iFGF13VY is not sufficient to replicate the iFGF-specific modulation of $\text{Na}_v1.5$ gating and function.** (A) Schematics of iFGF12B, iFGF13VY, and the iFGF chimeras generated with the iFGF12B and iFGF13VY N-termini exchanged (iFGF12B/13 and iFGF13VY/12). (B) Normalized inactivation, G-V, and VSD-IV F-V curves for $\text{Na}_v1.5$ expressed alone (grey dashed line), with iFGF12B (blue dashed line), iFGF13VY (orange dashed line), or one of the iFGF chimeras, FGF12B/13 (blue triangle) or FGF13VY/12 (orange diamond). The effects of the two iFGF chimeras on the G-V and F-V curves are distinct from those observed with either iFGF12B or iFGF13VY, implying that the N-termini of iFGF12B and iFGF13VY alone do not confer iFGF-specific regulation of $\text{Na}_v1.5$.

Downloaded from http://jgp.physiology.org/jgp/article-pdf/155/5/e202213300/1449616/jgp_202213300.pdf by Washington University in St. Louis Libraries user on 23 April 2023

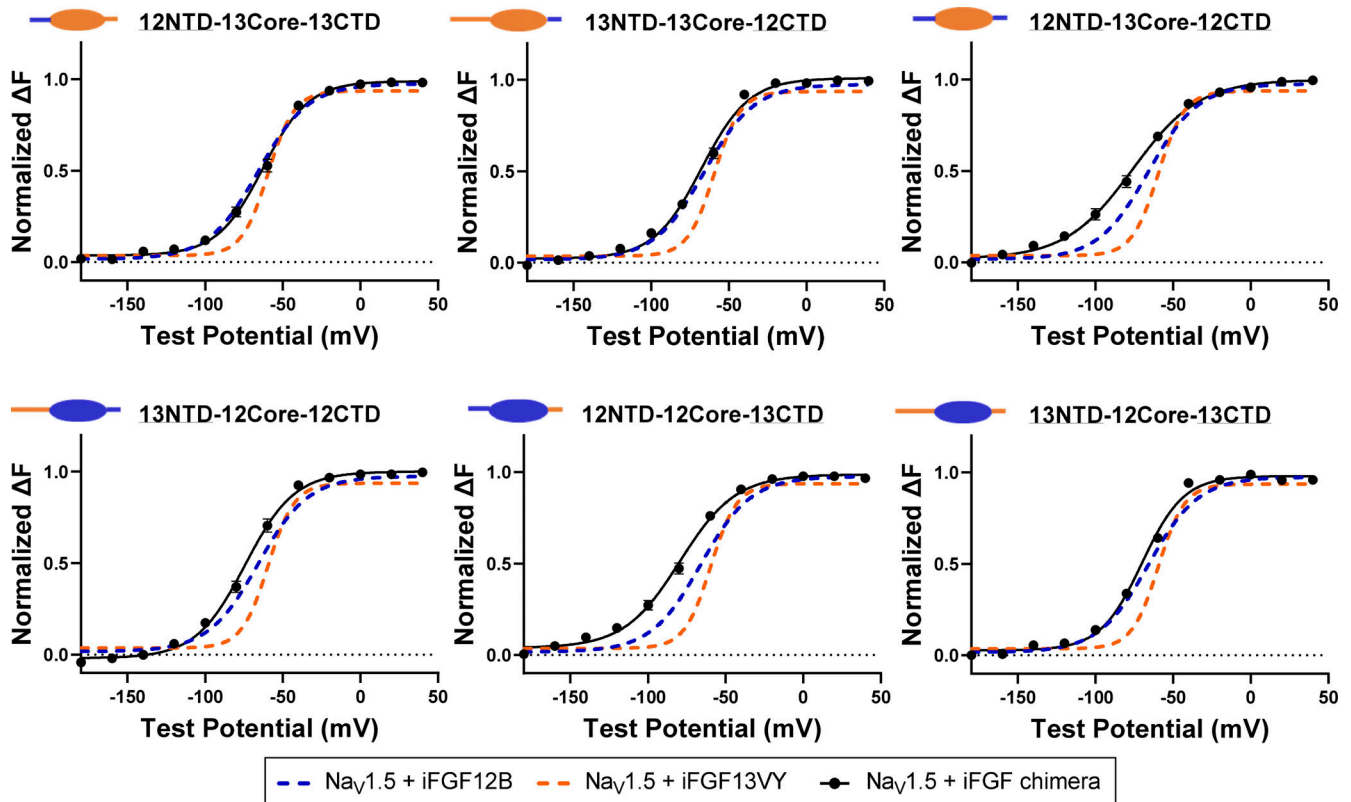


Figure S6. **iFGF chimeras differentially modulate the voltage dependence of VSD-IV activation (VSD-IV F-V).** Three pairs of iFGF chimeras were constructed by switching the various iFGF domains of iFGF12B and iFGF13VY: the N-termini (left), the C-termini (middle), and both the N- and C-termini (right). The VSD-IV F-V curves of the various iFGF chimeras (black circle) are plotted together with those of either iFGF12B (blue dashed line) or iFGF13VY (orange dashed line). The top row presents data for iFGF chimeras with the iFGF13VY core domain and the iFGF12B N- (left), C- (middle), or both N- and C-termini (right) exchanged, and the bottom row shows the reverse configurations, i.e., the iFGF12B core domain with the iFGF13VY N- (left), C- (middle), or both N- and C-termini (right) exchanged. In both cases, the exchanged domain(s) is (are) underlined. As is evident, none of these chimeras confer functional effects on the activation of VSD-IV identical to those seen with native iFGF12B or iFGF13VY.

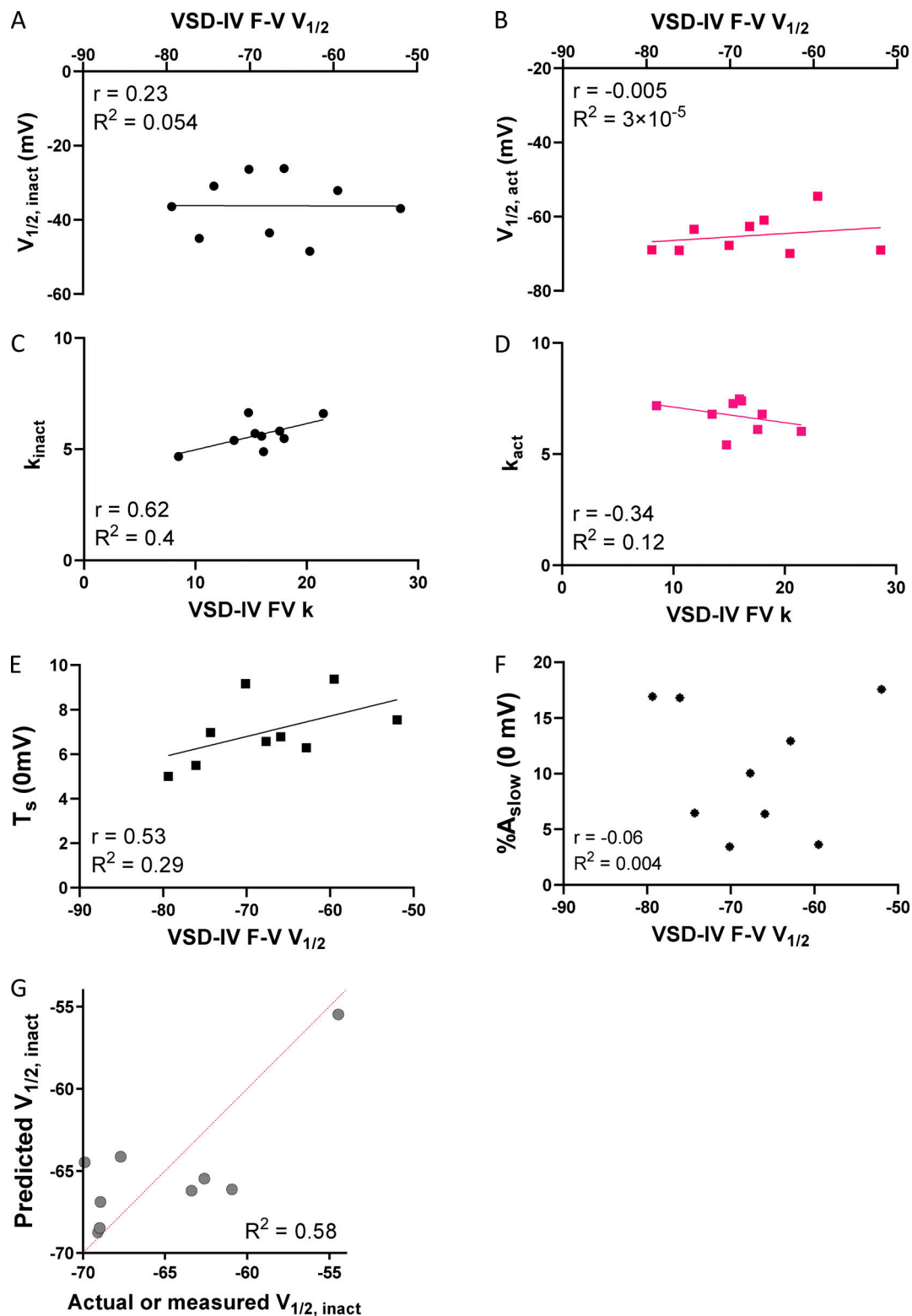


Figure S7. **Correlation and linear regression analyses reveal no correlations between the VSD-IV F-V and the G-V curves of activation and inactivation determined for $Na_v1.5$ coexpressed with iFGF12B, iFGF13VY, or the iFGF12B/13VY chimeras.** The data derived from the voltage-clamp and VCF recordings of $Na_v1.5$ coexpressed with iFGF12B, iFGF13VY, and the iFGF12B/13VY chimeras were plotted to determine if there were any correlations between the parameters ($V_{1/2}$ and k) derived from the Boltzmann fits to the VSD-IV F-V and the G-V curves. **(A and B)** As is evident in the plots shown, there are no correlations between $V_{1/2}$ determined from the VSD-IV F-V curves and the G-V curves for I_{Na} inactivation (A) or activation (B). **(C and D)** Comparison of the slope factors, k , of VSD-IV F-V and the G-V curves reveals a modest correlation for I_{Na} inactivation (C), but no correlation for I_{Na} activation (D). **(E and F)** In addition, the VSD-IV F-V $V_{1/2}$ values are not well correlated with either the slow inactivation time constants (E) or the fractional amplitudes of the slow component of I_{Na} decay (F). **(G)** The k and $V_{1/2}$ values, determined from the VSD-IV F-V curves, cannot be used to predict the inactivation G-V $V_{1/2}$ values.

Provided online are four tables. Table S1 lists primers used in screening *Fgf13* floxed (*Fgf13^{fl/+}* and *Fgf13^{fl/fl}*) and *cFgf13KO* mice. Table S2 lists biexponential fits to the decay phases of I_{Na} recorded at various test potentials from LV myocytes isolated from WT, *cFgf13KO*, and *cFgf13KO* + iFGF12B mice. Table S3 lists biexponential fits to the decay phases of I_{Na} evoked at various test potentials from oocytes expressing $Na_v1.5$ alone or $Na_v1.5$ combined with iFGF12B or iFGF13VY. Table S4 lists properties of I_{Na} recorded from *Xenopus* oocytes expressing $Na_v1.5$ in combination with iFGF chimeras.